# Chapter One

# Introduction

# Chapter One

# Introduction

## 1.1. Introduction

**Photo 1.1:** A colorful picture taken in 11 August 2002 from talk presented in Anchorage, Alaska, shows a spectacular Aurora borealis above. (Ref: http://www.phy6.org/Education/wstern.html (23/3/2006))

The Aurora is a luminous glow of the upper atmosphere in the form of majestic, colorful, and irregular lights in the night sky. The Aurora has a variety of shapes, colors, and structures, and also changes in time, which is caused by energetic particles that

enter the atmosphere from above. This definition differentiates Aurora from sky brightness that is due to reflected or scattered sunlight, as shown in photo 1.1.

When energetic charged particles enter the Earth's atmosphere from the solar Wind, but these energetic particles are mostly electrons, and protons also make Aurora. The energetic charged particles travel along magnetic field in helical path. The Earth's magnetic field looks like that of a dipole magnet where the field lines are coming out and going into Earth near its poles. The Auroral energetic charged particles are thus guided to the Earth's atmosphere by the Earth's magnetic field. As they penetrate into the upper atmosphere, the chance of colliding with an atom or molecule increases the deeper they go. Due to these collisions the atoms or molecules takes some of the energy of the energetic particle and make transition to excited states. When they make the transition back to their ground states they emit light characteristic of the atoms and molecules. But this process of emitting the light called Auroral light, [The Northern Light, Brekke, Egeland, 1983].

## 1.2. Regions of Aurora

Aurora ovals are the regions which the Aurora occurs in them, and the radius of these rings is roughly about (1400 - 1550) miles or (2252.6 km to 2493.95 km) around the Earth's magnetic poles , but these rings in general located between 65 and 75 degrees latitude in poles of the Earth. The Aurora occurs at a height of about 60 miles or (96.54 km) above the Earth's surface.

However these rings cover the two poles of the Earth, so that the Aurora that occurs in the southern hemisphere is named Aurora Australis, where as the Aurora that occurs in the northern hemisphere is named Aurora Borealis. Photo 1.2 shows a view of entire Auroral oval taken by Dynamic Explorer 1 satellite (DE-1).

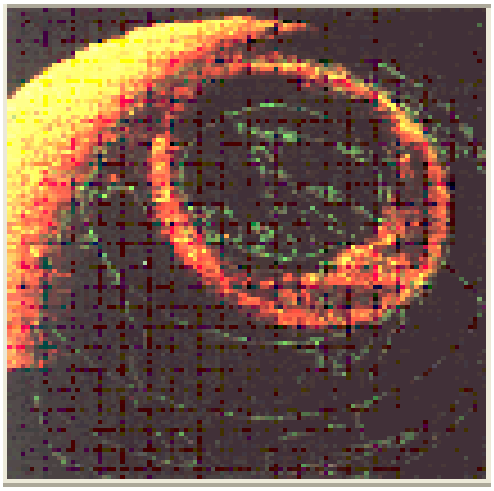

**Photo1.2**: Aurora observed by an imaging camera 8th November 1981 from high above the North Polar Region**.**

(Ref: http://www.albany.edu/faculty/rgk/atm101/Aurora.htm (19/3/2006))

## 1.3. Ionosphere and Magnetosphere

The Earth's atmosphere is a cloud of gas and suspended solids extending from the Earth's surface out many thousands of kilometers; it is conventionally divided into a number of regions, each where a significant chemical or physical change occurs. But these regions are included troposphere, stratosphere, mesosphere, and thermosphere. The ionosphere is the mixture of ions and electrons embedded in the thermosphere above around 90 kilometers. Above this height, the neutral density is sufficiently low that recombination times for ionized gas are long. Thus there exists not only the gas of ions and electrons, but also the possibility of electrostatic fields where the charge balance (number of ions/number of electrons) departs from unity. The charged particles are generally constrained to follow the magnetic field lines. At equatorial and mid-latitudes, the magnetic field lines are closed. Charged particles will drift with the field lines, and will tend to remain `trapped' in this region, the plasmasphere. At high latitudes, the magnetic field lines become connected to the interplanetary magnetic field

and are essentially open to the solar wind. This high-latitude ionosphere is thus very much more active than the low-latitude ionosphere, reflecting solar activity in the form of, for example Aurora, [Davies, Kenneth, Peter Peregrines Ltd .London, 1990].

The magnetosphere is the region surrounding the Earth where the Earth's magnetic field is stronger than the interplanetary field. And that is controlled by the Earth's magnetic field, but it is a dynamic region of flowing plasma guided by our magnetic field which at times connects into the Sun's magnetic field. Within the Earth's magnetosphere are found cold plasma from the Earth's ionosphere, hot plasma from the Sun's outer atmosphere, and even hotter plasma accelerated to great speeds which "rains" on our upper atmosphere causing Aurora in both the northern and southern hemispheres.

The Earth's magnetic field is like a dipole magnet only close to the surface. The Earth's magnetic field extends far out into space for thousands of miles. In order to provide some basic understanding of the shape of the Earth's magnetosphere, we must first discuss phenomena caused by the Sun. The extremely hot atmosphere of the Sun is plasma; that is a gas consisting of charged particles; mostly electrons and protons. Solar plasma streams radially into space at high speed and pull the Sun's magnetic field with it. The electrified particles and the solar magnetic field that they pull along for a ride is called the solar wind. These bits of the Sun come streaming at us at velocities of 450 km/second or more. Notice the magnetosphere that surrounds the Earth and extends far beyond the atmosphere into space. This region is the scene of dynamic interactions between the Sun and Earth plasmas. The bullet shape of the magnetosphere is the direct result when it is blasted by the solar wind. The solar wind compresses the Sunward side of the magnetosphere, and it drags out the night-side magnetosphere (into a magnetotail).This overall shape of the magnetosphere is illustrated in Figure 1.1.

The magnetopause separates the confined planetary magnetic field and magnetospheric plasma from the magnetized solar wind plasma in the magnetosheath. The location of the magnetopause is determined by a balance between the solar wind hydrodynamic pressure and the magnetic pressure of the compressed planetary magnetic field and is generally characterized by a discontinuity in the tangential component of the magnetic field. The long tail-like is seen in Figure 1.1 allows the ions (thermal plasma) to escape along these field lines in the tail, [Dessler and Michel, 1966; Bauer, 1966]. The outflow of plasma through regions of open ( or more generally tail-like ) magnetic field lines , resulting in a permanent escape of ions from the polar ionosphere is called polar wind , and the hydromagnetic model later proved that the out flow should be supersonic, [Axford, 1968].

## 1.4. The occurrence of Aurora

Before the charged particles entering the atmosphere, it is being captured by the Earth's magnetosphere. This is the region surrounding the Earth formed by the Earth's magnetic field. To imagine the magnetic field of Earth, think of Earth as a giant bar magnet with its poles more or less aligned with the geographic North and South poles of Earth. The magnetic field lines of this magnet form giant arches, stretching well outward into space, and connecting the poles. As the charged particles of the Solar Wind approach the magnetic field, they are forced to change their course, and begin a spiral motion along the lines of the magnetic field. On the side of the Earth facing the sun, the Earth's magnetosphere is "squashed" by the incoming Solar Wind. On the side of the Earth facing away from the Sun the magnetosphere becomes elongated. This happens when the Earth's magnetic field tries to hold the magnetosphere in place, while the Solar Wind tries to stretch it out. At the Earth's magnetic poles the Earth's magnetic field lines converge to form a "funnel" into which the trapped Solar Wind can be

channeled. The magnetic field lines "dressed" with the charged particles of the captured Solar Wind as shown in Figure 1.1, [Robert H., 1980].

Once through this "polar funnel" the Solar Wind begins to descend into the Earth's upper atmosphere. When these high speed charged particles enter the Earth's upper atmosphere, they collide with the atoms of the atmospheric gases (mostly oxygen and nitrogen). During such collisions electrons in atoms can be excited to higher energy levels within an atom, or even completely "kicked out" of an atom. The excited electrons emit energy in the form of light when they return to their original positions in their parent atoms. This emitted light forms the Aurora, [Theodore P. Snow, 1993].

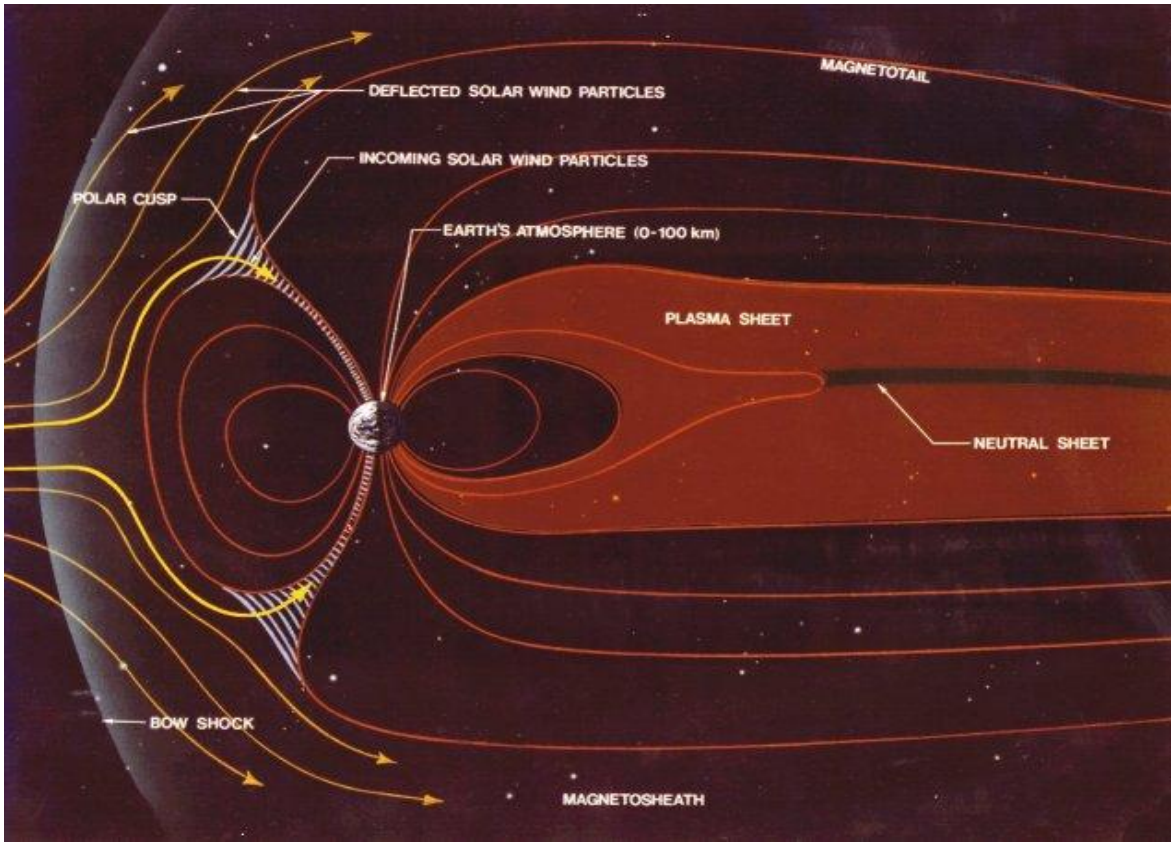


**Figure 1.1:** Solar wind enters the atmosphere according the polar funnel Region. (Ref: http://en.wikipedia.org/wiki/Image:Magnetosphere_schematic.jpg (11/3/2006))

The composition and density of the atmosphere and the altitude of the Aurora determine the possible light emissions. When an excited atom or molecule returns to the ground state, it sends out a photon with a specific energy. This energy depends on the type of atom and on the level of excitement, and we perceive the energy of a photon as color, [Robert H., 1980].

## 1.5. Activity of Aurora

Auroral activity depends on the activity of the sun. The more active is the Sun, the greater the number of Aurora. Where as the less active is the Sun the smaller the number of Aurora. But we know the activity of the sun goes in a periodic way and takes eleven years to change from high activity which called solar maxima to low activity which is called solar minima , and go back to solar maxima and so on,[Theodore P. Snow,1993] .

## 1.6. Previous Studies

Transversely accelerated ions at altitudes ranging from a few hundred kilometer to several Earth radii at Auroral and polar cusp altitudes have been observed [Klumpar *et al.,* 1984; Winningham and Burch, (1984); Arnoldy et al., 1992; Huddleston *et al.,* 2000; Moore *et al.,* 1999; Eklund *et al.,* 1997; Lundin et al., 1995; Arvelins *et al.,* 2005]. The ion acceleration through wave-particle interaction with plasma turbulence at high latitudes of the Earth's magnetosphere has been generally been accepted to explain the origin of the above observations. The effect of wave-particle interactions on ion outflow in the polar wind and Auroral region is a subject of intense investigations, because the escape of the ionospheric ions to the magnetosphere is an important ionosphere/magnetosphere coupling mechanism. Therefore several models have been

developed to study the ion outflow and to explain the observations of the non-Maxwelian features of $H^+$ and $O^+$ ion velocity distributions at high latitudes. [Chang and Coppi, 1981] suggested a mechanism by which wave-particle interactions of ions with intense turbulence near lower hybrid frequency leads to ion conic formation observed by satellite, and consequently the intense lower-hybrid waves that are detected along the discrete Auroral field lines could be the prime cause for the ion acceleration process. The plasma simulations of this mechanism [Retterer *et al.,* 1986] predicted the simulations occurrence of counter streaming electrons that are commonly observed in conjunction with the ion conics in the super Auroral region.

[Retterer *et al.,* 1987a,b] demonstrated that cyclotron resonance with observed electric field fluctuations is responsible for production of the oxygen-ion conic that are observed by the Dynamic Explorer 1 satellite in the central plasma-sheet region of the Earth's magnetosphere, they described the ion velocity distribution by a quasi-linear diffusion equation which is solved by the MC technique. [Crew *et. al.* 1990] presented a general theoretical treatment of energetic oxygen ion conics formation though cyclotron resonance with magnetospheric electromagnetic plasma turbulence, their theoretical predictions were found to be in excellent agreement with observations. [Retterer *et. al.,* 1994] interpreted the data from the rocket campaigns MARIE and TOPAZ III, within regions of low-altitude transversly accelerated ions, to explain the acceleration of the ions, they found that the observed electric field amplitudes are sufficient to explain the observed ion energies in the MARIE event.

The characteristics of non-Maxwellian ion velocity distributions have been observed in the polar wind and in the Auroral region, for example the supersonic nature of the polar wind and the asymmetry of the ion velocity distribution [Persoon *et al.,* 1983; Najai *et al.,* 1984; Biddle *et al.,* 1985], the upward flowing light and heavy ions

[Yau *et al.,* 1985; Peterson *et al.,* 1995], observed day/night asymmetry in the outflow of thermal $O^+$ in the polar cap [Horita *et al.,* 1993], and the availability of reliable measurements of thermal electron anisotropies [Yau *et al.,* 1995].

In a series of studies, [Barakat and Barghouthi, (1994a, b)], [Barghouthi and Barakat, (1995)], [Barghouthi, (1997), Barghouthi *et al.,* 1998, and Barghouthi and Atout, (2006)] used MC simulation to investigate the effect of wave-particle interaction on $H^+$ and $O^+$ outflows in the polar wind and Auroral region. They interpreted the effect of finite gyroradius is responsible for production of the $H^+$ and $O^+$ toroids at high altitudes equatorward of the cusp that are observed by TIDE and TIMAS ion instruments on board the polar spacecraft. They described the $O^+$ ion conics produced at $2R_E$ on the Auroral field lines by invoking the ion acceleration through wave-particle interaction (i.e. $O^+$ ions drift upward along geomagnetic field lines, they interact with electromagnetic turbulence and, consequently, get heated in the direction perpendicular to the geomagnetic field, the mirror force converts some of the ion energy gained in the perpendicular direction into parallel kinetic energy, these two effects combine to form an ion-conic distribution). Also they found that, the $O^+$ ions are preferentially heated owing to their mass and to the pressure cooker effect, the escape flux of $O^+$ was greatly enhanced while that of $H^+$ remained unchanged, both $H^+$ and $O^+$ ions are more energetic in Auroral region than in polar wind at most altitudes, and the effect of body forced is more important in the polar wind and for $O^+$ ions than it for Auroral region and the $H^+$ ions.

Another series of papers, [Bouhram *et al.,* [2002, 2003a, 2003b, 2004]] investigated the transverse heating and outflow of ions in the cusp/cleft region. [Bouhram *et al.,* 2002], studied the spatial properties of ionospheric ion outflows associated with perpendicular heating processes in the cusp using a conjunction study

from two satellites and ground radar system, they presented an event of low-energy outflowing $H^+$ and $O^+$ populations observed by the Hyperboloid experiment aboard Interball Auroral probe from 13,000 to 19,000 Km altitude, and these populations are observed over the day side morning polar cap. They discussed the contribution of different energization mechanisms to the ion heating as a function of altitude, they found that, since broadband, extremely low-frequency turbulence is available to pre-heat the ions up to non-thermal energies; Lower Huprid waves may provide additional energization up to KeV energies for $O^+$ ions at high altitude.

[Bouhram *et al.,* 2003a], developed a two-dimensional, MC, trajectory-based code for ion outflow from the day side cusp/cleft, which is associated with transverse ion heating, and they modeled the altitude dependence of ion cyclotron resonance heating from 1000 Km to 3 $R_E$ by a power law spectrum with an index $\alpha$, and a parameter $\omega_\circ$ that is proportional to the spectral density at a referenced frequency. They found that, any triplet of residence time of the ions when being energized, $\alpha$, and $\omega_\circ$ leads to a unique transport pattern feature of ion flows associated with a cusp/cleft ionospheric source. [Bouhram *et al.,* 2003b] used high-altitude (1.5-3 $R_E$) ion observation as constraints and the results of [Bouhram *et al.,* 2003a] are used to determine the altitude dependence of transverse ion heating during a significant number of the Interball-2 satellites. [Bouhram *et al.,* 2004], focused on the altitude dependence of oxygen ion conics in the day side cusp/cleft region, they combined oxygen data from the Akebono, Interball-2, and cluster satellites and followed the global development of the energetic (up to ~ 10 KeV) ion outflow over a continuous and broad altitude range up to about 5.5 $R_E$. They confirmed the results of [Bouhram *et al.,* 2003b], such as the fact that transverse ion heating in the cusp/cleft is height-integrated at radial distance below 4 $R_E$, the results inferred from cluster observations put forward evidence of a

saturation of both a transverse energization rate and ion gyroradii, and they interpreted these results in terms of finite perpendicular wavelength effects in the wave-particle interaction.

Recently, [Lemaire *et al.,* 2007], reviewed the modeling techniques from the earliest primitive approaches to the most current treatments that account for collision processes, non-Maxwellian distribution of multiple ion species, the role of photo electrons in controlling plasma outflow, and the early polar wind measurements. The generally accepted mechanism for these non-Maxwellian features is sort of wave-particle interactions, in this mechanism, as the ions drift upward along the geomagnetic field lines; they interact with the electromagnetic turbulence and consequently, get heated in the direction perpendicular to the geomagnetic field. The mirror force converts some of the gained ion energy in the perpendicular direction into parallel kinetic energy. These effects combine to form an ion-conic distribution. Theoretical studies and observations showed that the wave-particle interactions play an important role in determining the behavior of ion outflow, therefore the inclusion of the WPI effect in a self consistent manner requires the solution of global non-linear problem with coupling between mechanisms of rather different spatial and/or temporal scales. This is beyond the current mathematical and computational abilities.

[Barghouthi, 1997] obtained an altitude dependent diffusion coefficient and [Bouhram *et al.*, 2004] derived velocity dependent diffusion coefficient. In this study we will use a combined (altitude part from [Barghouthi, 1997] and the velocity part from [Bouhram *et al.,* 2004]) form for the diffusion coefficient to investigate the $H^+$ and $O^+$ ions outflow in the equatorward of the cusp. And also, in this work, we will develop a model for the velocity diffusion coefficient $D_\perp$, to be velocity dependent (based on the work of [Crew and Chang, 1985; Chang, 1993, and Retterer *et al.*, 1994]) and altitude

dependent (based on the work of [Barghouthi, 1997 and Barghouthi *et al.*, 1998]). We will use this developed model of the diffusion coefficient to study the effect of velocity and altitude dependent wave-particle interactions on $O^+$ and $H^+$ ions outflows in the Auroral region. Finally we compare between the three models for $D_\perp$ (model I, model II, and model III).

## 1.7. Statement of the Problem

Several mechanisms, wave-particle interactions [Chang and Coppi, 1981; Chang *et al.*, 1986; Retterer *et al.*, 1987a, b, 1994; Crew *et al.*, 1990; Barghouthi, 1997; Barghouthi *et al.*, 1998; Barghouthi and Atout, 2006, Bouhram *et al.*, 2003a, b, 2004], parallel potential drops [Lundin *et al.*, 1995], and Centrifugal acceleration [Ho *et al.*, 1994] have been suggested for investigating the energization of keV $H^+$ and $O^+$ ions in polar region, and to explain the non-Maxwellian features of ions outflows at high altitudes and high latitudes,. In this thesis, we are interested to compare between the simulation results of three wave-particle interactions models with observations, and to choose the best model that produce acceptable simulation results when compared to the corresponding observations**.**

# Chapter Two

# Theoretical Formulation

# Chapter Two

# Theoretical Formulation

## 2.1. The Boltzmann Equation

Plasma some times called the fourth state of matter. But it is far from being a clearly defined physical state and the only common feature in the various situations is that to some degree free charges (i.e ions, electrons, and neutral atoms) are present. The motion of these species under the effect of the influence of external forces (gravitational, electric, polarization and magnetic) and the interaction between them is very difficult to understand, but to describe each species in plasma, we can deal with a separate velocity distribution function, $f_s(\mathbf{v}_s, \mathbf{r}_s, t)$, which defined such that $f_s(\mathbf{v}_s, \mathbf{r}_s, t)\, d\mathbf{v}_s d\mathbf{r}_s$ represent the number of particles of species at time t which have velocity between $\mathbf{v}_s$ and $\mathbf{v}_s + d\mathbf{v}_s$ , and position $\mathbf{r}_s$ and $\mathbf{r}_s + d\mathbf{r}_s$ . The changing of the distribution function with respect to time (changing of $\mathbf{v}_s$ , $\mathbf{r}_s$ ) because of the net effect of many forces can be described by the well-known Boltzmann equation . [Schunk, 1977].

$$\frac{\partial f_s}{\partial t} + \mathbf{v}_s . \nabla f_s + [\mathbf{g} + \frac{e_s}{m_s}(\mathbf{E} + \frac{1}{c}\mathbf{v}_s \times \mathbf{B})] . \nabla_{vs} f_s = \frac{\delta f_s}{\delta t} \qquad (2.1)$$

Where ($\mathbf{g}$) is the acceleration of gravity, ($\mathbf{E}$) is the electric field, ($\mathbf{B}$) is the magnetic field, Where $e_s, m_s$ are the charge and the mass of the species $s$ respectively, $\frac{\partial}{\partial t}$ is the

time derivative, $c$ is the speed of light, ($\nabla$) is the coordinate space gradient, ($\nabla_{vs}$) is the velocity space gradient.

The quantity ($\frac{\delta f_s}{\delta t}$) represents the rate of change of $f_s(\mathbf{v}_s, \mathbf{r}_s, t)$ in a given region of phase space ($\mathbf{v}_s$ , $\mathbf{r}_s$) as a result of collisions . As far as the collisions and the inverse power potentials, is given by Boltzmann collision integral [Schunk, 1977]:

$$\frac{\delta f_s}{\delta t} = \sum_t \int d^3 v_t d\Omega g_{st} \sigma_{st}(g_{st}, \theta)[f_s' f_t' - f_s f_t] \qquad (2.2)$$

Where $d\Omega$ is the element of solid angle in the s particle reference frame, $\theta$ is the scattering angle, $g_{st}$ is the relative velocity of the colliding particles s and t, $d^3 v_t$ is the volume element in the velocity space, $\sigma_{st}(g_{st}, \theta)$ is differential scattering cross section, and the prime denote quantities evaluated after collision.

## 2.2. The Gravitational Force

Newton's law of gravity states that every particle in the universe attracts every other particle with a force that is directly proportional to the product of their masses and inversely proportional to the square of the distance between them, regardless of the medium that separates them. If an ion have mass (m) separated by a distance (r) from the Earth whose mass $M_e$, the gravitational force is:

$$\mathbf{F}(\mathbf{r}) = \frac{GM_e m}{r^2}\hat{\mathbf{r}} \qquad (2.3)$$

Where $G$ is a universal constant called the universal gravitational constant, $\hat{\mathbf{r}}$ is a unit vector directed from the center of the Earth to the ion, $M_e$ is the mass of the Earth, and the negative sign mean that the ion is attracted to the Earth by the gravitational force.

The acceleration of gravity, (**g**), which produced by gravitational force from the Earth on the ion is given by:

$$\mathbf{g} = \frac{\mathbf{F}}{m} = \frac{GM_e}{r^2}\hat{\mathbf{r}} \tag{2.4}$$

We can find the gravitational potential energy $\Phi_g(r)$ from the work done by a force:

$$W = -(\Phi_g - \Phi_{g_o}) = -\Delta\Phi(r) = -\int_{r_o}^{r} \mathbf{F}(\mathbf{r}).\, d\mathbf{r} \tag{2.5}$$

where $r_o$ and $r$ are the geocentric distance to the location of the ion, $\Phi_g$ and $\Phi_{g_o}$ represents the gravitational potential energy at altitudes $r_o$ and $r$, but from the above we can found the formula of gravitational potential energy as a function of $r$ by substitute F(r) from equation (2.3) into equation (2.5) to get:

$$\Delta\Phi_g(r) = -GM_e m\int_{r_o}^{r}\frac{dr}{r^2} = GM_e m\left(\frac{1}{r_o} - \frac{1}{r}\right) \tag{2.6}$$

But the previous expression applies to the Earth-ion system separated by r provided that $r > r_o > R_e$.

## 2.3. Polarized Electrostatic Field

When electrons and ions collide at above certain altitudes, cyclotron frequencies are larger than their frequenters; so the electrons and ions are forced to move along the geomagnetic field lines. But the gravity cause a slight charge separation occurred to the electrons, but the electrons due to small mass tending to reside on the top of the heavier ions. However, a polarization electrostatic field is occurred due to slight separation of charges, which in its role prohibits further charges separation, after that the electrons move with each other due to the gravity, temperature gradients and density. This motion is called ampipolar diffusion.

For simplicity we use many approximation to describe the outflow of plasma under the effect of polarization electric field, but the diffusion approximation we use is one of these approximations, also we neglect the wave phenomena and the flow of plasma is subsonic. In addition, the net zero current conditions prevail due to the move of electrons and ions with each other, and we ignore the heat flow, there fore the momentum equation of the electrons become as [Schunk and Nagy, 2000]:

$$\nabla_{\parallel} p_e + \left(\nabla . \boldsymbol{\tau}_{\mathbf{e}}\right)_{\parallel} + n_e e \mathbf{E}_{\parallel} - n_e m_e \mathbf{g}_{\parallel} = n_e m_e \upsilon_{ei} \left(\mathbf{u}_i - \mathbf{u}_e\right)_{\parallel} + n_e m_e \upsilon_{en} \left(\mathbf{u}_n - \mathbf{u}_e\right)_{\parallel} \qquad (2.7)$$

where $\mathbf{E}_{\parallel}$ is the polarization electrostatic field that develops due to the very slight charge separation, $p_e$ is electrons partial pressure, $n_e$ is electrons density, $m_e$ is the mass of electron, $\mathbf{g}_{\parallel}$ is the component of acceleration due to gravity along the geomagnetic field lines, $\boldsymbol{\tau}_e$ is electrons stress tensor, $\upsilon$ is the collision frequency, $\upsilon_{en}$ is the electrons and neutral atoms collision frequency at the moment of collision and, $\mathbf{u}_i$ and $\mathbf{u}_{\mathbf{e}}$ are the drift velocity of ions and electros respectively.

An explicit expression to the electric field in many application cause the movement of electrons are needed to get the electrostatic potential $\left(\mathrm{V}_E\right)$, but how we can find this field ? We can find this by using equation (2.7) under some conditions which are: the electron–ion collision term is dropped due to small mass of the electron, and also every term containing $m_e$ is neglected so equation (2.7) is become as:

$$e\mathbf{E}_{\parallel} = -\frac{1}{n_e} \nabla_{\parallel} \mathrm{P_e} \qquad (2.8)$$

The expression is valid regardless of the number of ion species in the plasma.

It is valid to write $\mathbf{E}_{\parallel} = -\nabla_{\parallel} \mathrm{V}_E\left(r\right)$, due to alternate form of isothermal electron gas, and letting $\mathbf{E}_{\parallel} = -\nabla_{\parallel} \phi$ and $P_e = n_e k T_e$; where $\phi$ is the potential energy to the

polarization electric field and assuming that $T_e$ is constant, so we can write equation (2.8) as:

$$\frac{e}{kT_e}\frac{\partial \mathrm{V}_E(r)}{\partial r} = \frac{1}{n_e}\frac{\partial n_e}{\partial r} \tag{2.9}$$

Where $r$ is the spatial coordinate either along or perpendicular to geomagnetic field ($\mathbf{B}$). However to find the electrostatic potential $(\mathrm{V}_E)$, we treat equation (2.9) by integrating it and the result is called Boltzmann relation:

$$n_e = (n_e)_o e^{\frac{e\mathrm{V}_E}{kT}} \tag{2.10}$$

Where $(n_e)_o$ is the equilibrium electron density that prevails when $\mathrm{V}_E = 0$. But now we can write the electrostatic potential $(\mathrm{V}_E)$ as:

$$\mathrm{V}_E(r) = \frac{kT_e}{e}\ln\left(\frac{n_e}{(n_e)_o}\right) \tag{2.11}$$

Due to this the polarization electrostatic potential energy $\Phi_E(r)$ becomes:

$$\Phi_E(r) = kT_e \ln\left(\frac{n_e}{(n_e)_{\mathrm{o}}}\right) \tag{2.12}$$

Therefore to summarize the final potential energy profile $\Phi\,(r)$ due to gravity and polarization electric field, we return to the above two sections, the potential energy causing body forces (i.e. gravitational and polarization electrostatic) which is given by [Barakat and Schunk, 1983]:

$$\Phi(r) = kT_e \ln\left(\frac{n_e}{(n_e)_o}\right) + GM_e m\left(\frac{1}{r_o} - \frac{1}{r}\right) \tag{2.13}$$

## 2.4. Charged Particles in a Magnetic Field

It is known that when an ion with charge (q) moves with velocity **v** in a uniform magnetic field will be acted on by a famous force called Lorentz force, which is represented in Gaussian system of units as:

$$\mathbf{F} = \frac{q}{c}\mathbf{v} \times \mathbf{B} \tag{2.14}$$

where $c$ is the speed of light. When a positive ion moves perpendicularly to a uniform magnetic field $\mathbf{B_o}$, the direction of ions velocity can be change due to Lorentz force only, so we will note the ion exhibit in a circular motion about the uniform magnetic field, the radius of that path is known Larmor radius (gyro radius), and it can be computed by equating between Lorentz force and centrifugal force to give:

$$a_L = \frac{mc}{q}\frac{v_\perp}{B} \tag{2.15}$$

The Larmor frequency (gyro radius) is known as:

$$\Omega_c = \frac{qB_0}{mc} \tag{2.16}$$

However, the path of positive ion in a uniform magnetic field is shown in Figure 2.1:

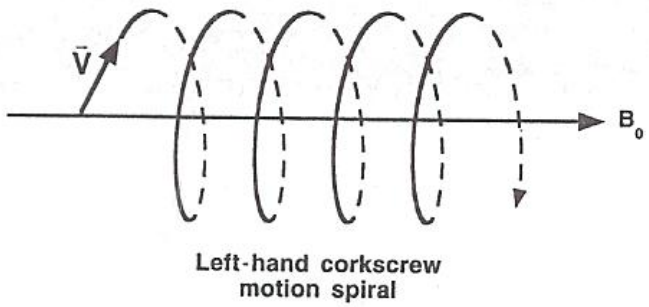


**Figure 2.1:** helical path Motion of a charged particle in a uniform magnetic field [Tsurutani, and Lakhina, 1997].

The ion velocity vector can be analyzed into two orthogonal components one parallel to $\mathbf{B_o}$ which represented by $\mathbf{v}_{\parallel}$ , and the other perpendicular to $\mathbf{B_o}$ which represented by $\mathbf{v}_{\perp}$ , so we can write it such that:

$$\mathbf{v} = \mathbf{v}_{\parallel} + \mathbf{v}_{\perp} \tag{2.17}$$

Assume there are no forces exerted on the ion which enters the uniform magnetic field: in the parallel direction; this implies that the ion moves unimpeded with a constant $v_{\parallel}$ along the uniform magnetic field. There is a cyclotron motion associated with the $v_{\perp}$ as shown in the Figure 2.1. Although the direction of perpendicular velocity $v_{\perp}$ changing continuously, the magnitude of $v_{\perp}$ remains unchanged in a uniform magnetic field as shown in the previous Figure 2.1. by using Lorentz force the positive ion gyrates in an opposite direction of gyration for negative ion. Since the positive ion gyrates in a left-hand sense relative to the uniform magnetic field , independent of whether they are moving along the uniform magnetic field or anti parallel to it, but the central field lines about which the ion gyrates is known guiding center .

However, if there is a strong magnetic field gradient in certain region the ion mirrored by Lorentz force. At the moment in time when the ions is being mirrored, then $v_{\perp} = v$ and $v_{\parallel} = 0$, which means all of its velocity is in the perpendicular to the magnetic field. The Lorentz force has a component toward the left, which leads the ion to accelerate in a direction anti parallel to the magnetic field. But the Lorentz force effects in a direction perpendicular to velocity vector, also there is no work done on the ion and the total energy of the ion remains constant as shown in the following equation:

$$E_T = \frac{1}{2}mv^2 = \frac{1}{2}mv_{\parallel}^2 + \frac{1}{2}mv_{\perp}^2 = E_{\parallel} + E_{\perp} \tag{2.18}$$

Where $E_T$, $E_{\parallel}$ and $E_{\perp}$ are the total, parallel and perpendicular kinetic energy of the ion respectively.

However, for ion moves from left to right in a constant magnetic field, the gradient as shown in Figure 2.2, when $E_{\perp}$ decreases, $E_{\parallel}$ increases , due to $E_{\perp}$ is keeping constant. The mirror point is reached, at $E_{\perp} = E_T$ and $E_{\parallel} = 0$, then the ion starts to be mirrored and so with $E_{\perp}$ decreasing and $E_{\parallel}$ increasing. By the mirror force the ion will be trapped due to a magnetic field lines and will bounce back and forth between mirror points [Tsurutani and Lakhina, 1997].

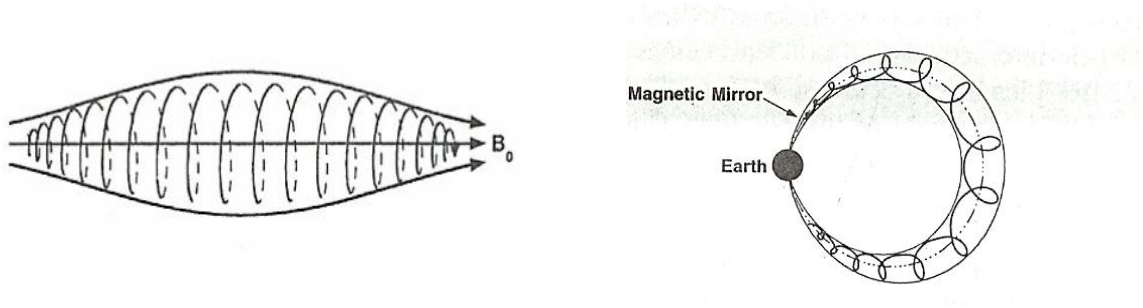


**Figure 2.2:** Magnetic bottles for plasma particles [Tsurutani and Lakhina, 1997]

## 2.5. The Wave Particle Interactions (WPI)

The stability of plasma that is found in the Auroral region and polar cap was the subject of many theoretical investigation; the results found that plasma is unstable with respect to the variety of waves [Barakat and Schunk, 1989]. In the Auroral region, the observed levels of the electromagnetic turbulence occurred over the polar cap [Gurnett and Inan, 1988].

The effects of WPI are represented by particle diffusion in the velocity space is [Retterer *et al.,* 1987a]:

$$\left[\frac{\partial f}{\partial t}\right]_{WPI} = \left(\frac{1}{v_\perp}\right)\frac{\partial}{\partial v_\perp}\left[D_\perp v_\perp \frac{\partial f}{\partial v_\perp}\right] \tag{2.19}$$

Where ($D_\perp$) is the quasi-linear velocity diffusion rate perpendicular to geomagnetic field lines and is given by the following expression [Retterer *et al.*, 1987b]:

$$D_\perp = \frac{q^2}{m^2}\sum_{n=-\infty}^{\infty}\int\frac{d\omega}{2\pi}\int\frac{d^3K}{(2\pi)^3}\left[\frac{n\Omega}{\omega}\right]^2 A_n \pi\delta\left(\omega - n\Omega - k_\parallel v_\parallel\right) \tag{2.20}$$

with

$$A_n = \frac{1}{2}J_{n-1}^2\left|E_L\right|^2(k,\omega) + \left[\frac{v_\parallel J_n^2}{v_\perp}\right]^2\left|E_\parallel\right|^2(k,\omega) + \frac{1}{2}J_{n+1}^2\left|E_R\right|^2(k,\omega) \tag{2.21}$$

In these equations, q is the ions charge, m is the ions mass, ($\Omega$) is the ion gyrofrequency, ($\omega$) is the angular frequency of the electromagnetic turbulence, **K** is the wave vector, $J_n = J_n\left(\frac{k_\perp v_\perp}{\Omega}\right)$ is the standard Bessel function, and $\left|E_L\right|^2$ and $\left|E_R\right|^2$ are the spectral densities of the electric field in the two perpendicular polarizations. [Retterer *et al.*, 1987b] assumed $\left(k_\parallel v_\parallel << \Omega\right), n = 1$ and $\left(\frac{k_\perp v_\perp}{\Omega} << 1\right)$, and found that :

$$D_\perp = \frac{\eta q^2}{4m^2}\left|E_x(\omega = \Omega)\right|^2 \tag{2.22}$$

where $\left|E_L\right|^2(\omega) = \eta\left|E_x\right|^2(\omega)$ , $\left|E_x\right|^2$ is the measured spectral density of the electromagnetic turbulence, and $\eta$ is the proportion of the measured spectral density by plasma wave instrument (PWI) on board the DE-1 space craft that corresponds to the left hand polarized wave. This velocity diffusion rate, $(D_\perp)$, given in equation (2.20) is independent of velocity, and it depends on position (altitude) through the variation of the ion gyrofrequency, $\Omega$, along the geomagnetic field lines. To improve the altitude

dependence of $(D_{\perp})$. [Barghouthi, 1997; Barghouthi *et al.,* 1998] processed the data collected by PWI on board the DE-1 space craft; they obtained the following expressions for $D_{\perp}$ in the region equatorward of the cusp.

$$D_{\perp}(r) = \begin{cases} 4.45\times10^{7}(r/R_E)^{7.95} cm^2 \sec^{-3}, & \text{for } H^+, \\ 6.94\times10^{5}(r/R_E)^{13.3} cm^2 \sec^{-3}, & \text{for } O^+. \end{cases} \quad (2.23)$$

However, the adoption of this altitude dependent diffusion coefficient and similar ones such as the adopted by [Crew et al., 1990; Barghouthi, 1997, and Barghouthi *et al.,* 1998] results in unrealistically high ion temperatures at high altitudes and did not produced the above observations of non-Maxwellian features at middle (~ 4 $R_E$) and high (~ 8 $R_E$) altitudes, such as $H^+$ and $O^+$ ion toroids and $H^+$ and $O^+$ ions temperature. The description of these non-Maxwellian features requires a velocity dependent diffusion rate as suggested by [Retterer *et al.,* (1994)].

The following three approaches, suggested different forms for the velocity dependence of the diffusion coefficient $D_{\perp}$.

## 2.3.1 Model I: The RCC model

Alternatively, the velocity dependence of the diffusion coefficient, $D_{\perp}$, may be estimated by using the frequency spectrum observations. Based on these observations, [Crew and Chang, 1985] suggested the following form for the velocity dependence of the velocity diffusion coefficient:

$$D_{\perp}(v_{\perp}) \; \alpha \; \left(\frac{v_{\perp}}{v_o}\right)^{\beta}\left[1+\left(\frac{v_{\perp}}{v_o}\right)^{\beta+1}\right]^{-1} \quad (2.24)$$

Where $v_o$ is the reference phase velocity; and $\beta$ is a parameter that depends on the shape of the spectrum curve and is chosen to be unity according to [Chang, 1993]. To model the wave-particle interactions process, we specify a model for the diffusion

coefficient, $D_{\perp}$, as a function of perpendicular velocity based on the work of [Crew and Chang, 1985); Chang 1993], and position along the Auroral geomagnetic field lines based on the work of [Barghouthi, 1997; Barghouthi *et al.*, 1998]. Accordingly, the above perpendicular diffusion coefficients, $D_{\perp}(\mathrm{O}^{+})$ and $D_{\perp}(\mathrm{H}^{+})$ are modified to be function of altitude and velocity, and given by:

$$D_{\perp}(H^{+}) = 4.45\times10^{7}(r/R_{E})^{7.95}\left(\frac{v_{\perp}}{v_{o}}\right)\left[1+\left(\frac{v_{\perp}}{v_{o}}\right)^{4}\right]^{-1} \qquad (2.25)$$

$$D_{\perp}(O^{+}) = 6.94\times10^{5}(r/R_{E})^{13.3}\left(\frac{v_{\perp}}{v_{o}}\right)\left[1+\left(\frac{v_{\perp}}{v_{o}}\right)^{4}\right]^{-1} \qquad (2.26)$$

These diffusion coefficients are altitude and velocity dependent, and they will be used to investigate the effects of altitude and velocity dependent wave-particle interactions on the $O^{+}$ and $H^{+}$ ions outflow in the Auroral region.

### 2.3.2 Model II: The Bouhram model

[Bouhram et al., (2004)] obtained the velocity dependent diffusion coefficient, $D_{\perp}$, they found:

$$D_{\perp}\alpha\, \mathrm{J}^{2}{}_{\circ}\left(k_{\perp\circ}\rho_{i}\right) = \mathrm{J}^{2}{}_{\circ}\left(\frac{k_{\perp\circ}v_{\perp}}{\Omega_{i}}\right) = \mathrm{J}^{2}{}_{\circ}\left(\frac{2\pi\, v_{\perp}}{\lambda_{\perp\circ}\Omega_{i}}\right) \qquad (2.27)$$

Where ($\rho_{i} = v_{\perp}/\Omega_{i}$) denotes the ion gyroradius, ($k_{\perp}$) is the perpendicular component of the wave vector (**K**) , ($\Omega_{i}$) is the ion gyrofrequency, and ($\mathrm{J}_{\circ}$) is the zeroth order of standard Bessel function. Therefore, to model the ion perpendicular heating process, we specified a model for ($D_{\perp}$) as a function of perpendicular velocity ($v_{\perp}$) and position ($r/R_{E}$) along the geomagnetic field line. For the velocity dependence, we chose the above form obtained by [Bouhram et al., (2004)], while for the altitude dependence we

chose the form calculated by [Barghouthi (1997)]. Altogether, the velocity and altitude dependent diffusion coefficient rate is written:

$$D_{\perp}(r, v_{\perp}) = \begin{cases} 4.45\times10^{7}(r/R_E)^{7.95}\mathrm{J}^2{}_{\circ}\left(\dfrac{2\pi\, v_{\perp}}{\lambda_{\perp}{}_{\circ}\Omega_i}\right) cm^2\ \mathrm{sec}^{-3}, & \text{for } \mathrm{H}^+, \\ 6.94\times10^{5}(r/R_E)^{13.3}\mathrm{J}^2{}_{\circ}\left(\dfrac{2\pi\, v_{\perp}}{\lambda_{\perp}{}_{\circ}\Omega_i}\right) cm^2\ \mathrm{sec}^{-3}, & \text{for } \mathrm{O}^+. \end{cases} \tag{2.28}$$

Since the data collected by the PWI instrument do not include information about $\lambda_{\perp}$, and detailed information about $\vec{k}$-spectrum of the electromagnetic turbulence is un available. Owing to this, we considered a wide range of characteristic wavelengths for electromagnetic turbulence [$\lambda_{\perp}$= $\infty$, 100, 10,1 km]. However The boundary conditions selected for the Auroral region are similar to those of [Barghouthi (1997)], and the procedure of simulation as mentioned in the RCC model in the above.

### 2.3.3 Model III: Barghouthi model

[Retterer *et al*., 1987b] assumed $k_{\perp}v_{\perp} << \Omega$ (i.e. the ion Larmor radius $a_L$ to be much less than the perpendicular wavelength $\lambda_{\perp}$ of the electromagnetic turbulence). However, as an ion drift upward along a geomagnetic field lines, it heats up due to WPI, and geomagnetic field intensity (**B**) decreases, the combined effect of these two factors results in a rapid increases in $a_L$ with altitude. At higher altitudes, the larmor radius $a_L$ may become comparable to or even more than $\lambda_{\perp}$ and consequently $\left(\dfrac{k_{\perp}v_{\perp}}{\Omega}\right)$ becomes greater than one, and hence the velocity independent expression for $D_{\perp}$ given in equation (2.22) becomes in accurate. At these altitudes, [Barghouthi, 1997] and [Barghouthi *et al*.,1998] modify the form of the diffusion coefficient $D_{\perp}$. To do this,

they divide the general form of $D_{\perp}$ as given in equation (2.20) by the simplified form given in equation (2.22) to obtain a ratio denoted by R:

$$R = \frac{\frac{q_i^{\,2}}{m_i^{\,2}} \sum_{n=-\infty}^{\infty} \int \frac{d\omega}{2\pi} \int \frac{d^3K}{(2\pi)^3} \left[\frac{n\Omega}{\omega}\right]^2 A_n \pi \delta\left(\omega - n\Omega - k_{\parallel} v_{\parallel}\right)}{\frac{\eta q_i^{\,2}}{4m_i^{\,2}} \left|E_x(\omega = \Omega)\right|^2} \qquad (2.29)$$

They plot the ratio R against the argument of Bessel function $\left(\frac{k_{\perp} v_{\perp}}{\Omega}\right)$ as shown in Figure (2.3), when the argument $\left(\frac{k_{\perp} v_{\perp}}{\Omega}\right)$ is less than 1, the ratio R is 1 which means that ($D_{\perp}$) needs no modification, and they reproduce [Retterer et al., 1987] form, but as the argument $\left(\frac{k_{\perp} v_{\perp}}{\Omega}\right)$ becomes greater than one then the ratio decreases as $\left(\frac{k_{\perp} v_{\perp}}{\Omega}\right)^{-3}$. Therefor when $\left(\frac{k_{\perp} v_{\perp}}{\Omega} \geq 1\right)$ they need to multiply ($D_{\perp}$) given in equation (2.23) by $\left(\frac{k_{\perp} v_{\perp}}{\Omega}\right)^{-3}$. The modified form of the diffusion coefficient is consistent with the suggested form given by [Crew , and T chang, 1985] and is given by:

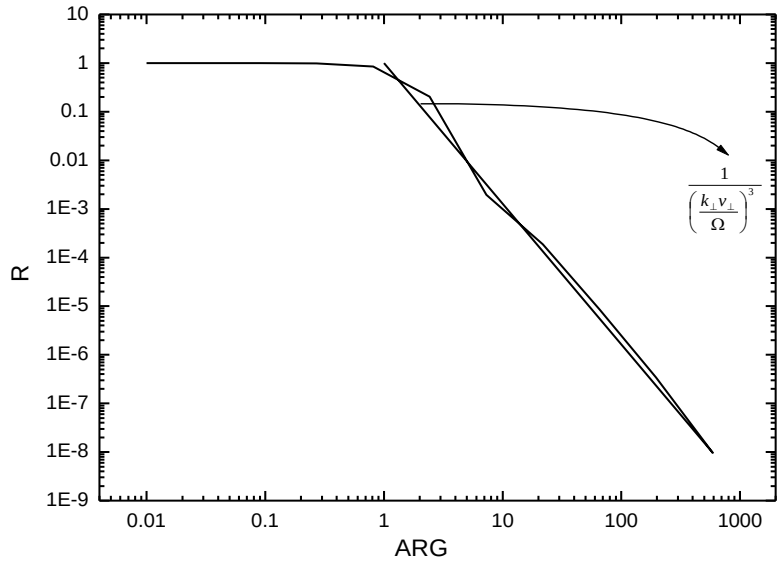


**Figure 2.3:** The ratio of R versus the ARG.

$$D_\perp(r, v_\perp) = D_\perp(r)\begin{cases} 1 & \text{for } \left(\frac{k_\perp v_\perp}{\Omega}\right) < 1 \\ \varepsilon^{-3} = \left(\frac{k_\perp v_\perp}{\Omega}\right) & \text{for } \left(\frac{k_\perp v_\perp}{\Omega}\right) \geq 1 \end{cases} \qquad (2.30)$$

Where $D_\perp(r)$ is given in equations (2.23).

## 2.6. The Boundary conditions

In the simulation, we study the steady state flow of a fully ionized plasma ($H^+$, $O^+$, and electrons) along the geomagnetic field lines in the high-altitude top side ionosphere (i.e., the Auroral region). The ions move under the effect of body forces (i.e., due to gravitational and polarization electrostatic fields) and mirror force due to the divergence of the geomagnetic field. During their motion, the ions interact with the electromagnetic turbulence. The simulation region is a geomagnetic tube extending

from the exobase at 1.2 $R_E$ to 10 $R_E$. The geomagnetic field was taken to be proportional to $r^{(-3)}$, where r is the geocentric distance. In the absence of wave-particle interactions, the ion motion can be described by Liouville theorem [Barakat and Schunk, 1983], conservation of energy, conservation of the first adiabatic invariant ($\eta$) and the ion velocity distribution function at the exobase, we can calculate the ion velocity distribution at any point in the simulation region for a given potential energy profile ($\phi$). The resulting relation can be solved simultaneously with the expression for ($\phi$) and the quasi-neutrality condition:

$$\Phi(r) = kT_e \ln\left(\frac{n_e}{(n_e)_o}\right) + GM_e m\left(\frac{1}{r_\circ} - \frac{1}{r}\right) \qquad (2.31)$$

$$n_e \cong n(O^+) + n(H^+) \qquad (2.32)$$

Where K is Boltzmann's constant, $T_e$ is electron temperature, $n_e$ and ($n_{e\circ}$) are the electron densities at r and ($r_\circ$), respectively, G is the universal gravitational constant, $M_E$ is the mass of the Earth, and m is the ion mass.

The boundary conditions selected for the Auroral region are similar to those of [Barghouthi, 1997], at lower boundary (1.2 $R_E$) we set the $H^+$ ion drift velocity at $16\times10^5\, cm\,\mathrm{sec}^{-1}$, the $H^+$ ion density at $100\, cm^{-3}$, and the $H^+$ ion temperature at the lower boundary at $0.2\, e\mathrm{V}$. At the lower boundary, we set the $O^+$ ion drift velocity at $0\, cm\,\mathrm{sec}^{-1}$, the oxygen ion density at $5000\, cm^{-3}$, and the $O^+$ ion temperature at $0.2\, e\mathrm{V}$. The electron temperature was kept constant at $1000^o K$ along the entire simulation tube (1.2 $R_E$ – 10 $R_E$). We also assume the velocity distribution to be a drifting Maxwellian for $H^+$ ions and the up going half of non - drifting Maxwellian for $O^+$ ion.

An ion is injected into the simulation region at the lower boundary (1.2 $R_E$) with a random initial velocity that corresponds to the assumed ion velocity distribution immediately below the lower boundary. The injected ion is considered to move for a short interval of time $\Delta t$ under the influence of the body forces (gravitational and polarization electrostatic), and geomagnetic field. The potential energy due to the body forces is given by [Barghouthi, 1997]:

$$\Phi(r) = kT_e \ln\left(\frac{n_e}{(n_e)_o}\right) + GM_e m\left(\frac{1}{1.2R_E} - \frac{1}{r}\right) \qquad (2.33)$$

Where $k$ is Boltzmann's constant; $T_e$ is the electron temperature; and $n_e$ and $n_{e\circ}$ are the electron densities at $r$ and 1.2 $R_E$, respectively, which can be calculated from the quasi-neutrality condition [$n_e$ = n ($O^+$) + n ($H^+$)]. $G$ is the gravitational constant, $M_E$ is the mass of the Earth, and m is the ion's mass (i.e., $H^+$ or $O^+$). The geomagnetic field **B** was taken to be proportional to $r^{-3}$, where $r$ is the geocentric distance. The effect of wave-particle interactions during the period $\Delta t$ is taken into account by perturbing the ion's perpendicular velocity by a random increment $\Delta v_\perp$ such that:

$$\left\langle (\Delta v_\perp)^2 \right\rangle = 4D_\perp \Delta t \qquad (2.34)$$

Where $D_\perp$ is given by equation (2.25) for $H^+$ ions, and equation (2.26) for $O^+$ ions.

The above procedures are repeated until the injected ion exits the simulation region at either ends 1.2 $R_E$ or 10 $R_E$, and then another ion is injected at 1.2 $R_E$. The injected ions ($10^6$), one at a time, are monitored as they cross a chosen set of altitudes. At each altitude, we used a 2-D grid whose coordinates are the velocities parallel and perpendicular to the geomagnetic field **B**. The time spent by the ions in a given velocity bin, divided by the bin's volume, is proportional to the value of the velocity distribution at the center of the bin. Moreover, the velocities of the injected ions, as they cross:

monitoring altitude, are used to compute the moments of the velocity distribution at that altitude. The moments considered here are defined as follows:

$$n_i = \int f_i d^3 v_i \tag{2.35}$$

$$u_i = \frac{1}{n_i} \int v_{i\parallel} \; f_i d^3 v_i \tag{2.36}$$

$$T_{i\parallel} = \frac{m_i}{n_i k} \int \left( v_{i\parallel} - u_i \right)^2 f_i d^3 v_i \tag{2.37}$$

$$T_{i\perp} = \frac{m_i}{2 n_i k} \int v_{i\perp}{}^2 \, f_i d^3 v_i \tag{2.38}$$

In equations (2.35)-(2.38), *i* denotes the type of the ion ($H^+$ or $O^+$) and, $n_i$, $u_i$, $T_{i\parallel}$ , and $T_{i\perp}$ are the ion density, drift velocity, parallel temperature, and perpendicular temperature, respectively.

# Chapter Three

# Monte Carlo Simulation

# Chapter Three

# Monte Carlo Simulation

## 3.1. Introduction

MC methods are a widely used class of computational algorithms for simulating the behavior of various physical and mathematical systems. They are distinguished from other simulation methods by being stochastic technique which means that they are based on the use of random numbers and probability statistics to investigate problems.

MC method is used in modeling of physical problems which allows us to examine the complex systems by solving the equations which describe the interactions between two ions ; where as the interactions between thousands or millions of ions is impossible but by using this method large systems can be examined and the system is described as a whole.

## 3.2. MC Simulation technique to solve Boltzmann's Equation

MC method is a powerful technique to solve Boltzmann's equation by a particle simulation. MC is a simple concept, goes in straight forward algorithm, and we can used MC to include new features such as different collisions models, electric field, gravity and geomagnetic field, which makes it the best technique are used in the space plasma physics, there fore we used it to solve Boltzmann's equation to find the velocity distribution function and the moments of the ions (density $n_i$, drift velocity $u_i$, parallel temperature $T_{\parallel i}$, and perpendicular temperature $T_{\perp i}$).

We can do the simulation to the motion of the ion in the region (Aurorarl region ) we choose it which no collisions between ions are included as follow, we assume the steady sate flow of three components plasma composed of $H^+$, $O^+$ and electrons, the simulation region considered to be a geomagnetic tube extending from $r_o = 1.2R_e$ to $r = 10R_e$, as shown in the Figure 3.1.

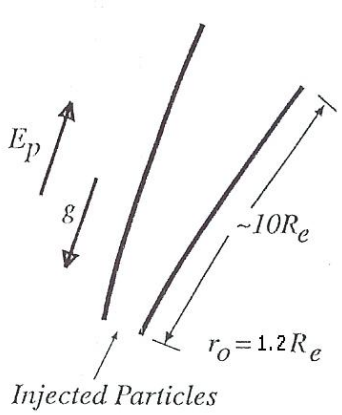


**Figure 3.1:** A schematic representation of the model considered by MC method [Barakat and Barghouthi, 1994b].

We injected the ion at $r_o$ with velocity drifting Maxwellian distribution function, the ion is considered to move for a short interval of time ($\Delta t$) under the influence of geomagnetic field, polarization electric field, gravity and the effect of wave particle interaction. The geomagnetic field was considered to be proportional to $r^{-3}$, where r is the geocentric distance. However, a suitable grid in the velocity space is used to register the ions behavior, but the velocities of the test ions that they cross one of the monitoring altitude can be used directly to calculate the moments of the distribution functions at that altitude. Then the time an ion taken it in each bin divided by the bins volume is considered to proportional to the ion velocity distribution function at the center of the bin.

The procedure we discussed it in the above is repeated until the test ion exist the simulation region we chosen it in the above. Then another test ion initiated at the bottom of the region and we remain do the above until the ions we taken it are finished. One of the monitoring altitudes at each altitude a suitable grid is used to registor the behavior of test ions, but here we used tow dimention (2-D) grid velocities whose coordinates are parallel and perpendicular to the geomagnetic field .

As we mentioned in the above, the time, an ion taken it in each bin divided by the bin's volume is considered to proportional to the ion velocity distribution function at the center of the bin. The time interval ($\Delta t$) should be taken small enough so that the velocity of the test ion, and consequently, during time interval ($\Delta t$). But the computational resources we used it impose a limitations on how the time interval ($\Delta t$) can be chosen.

## 3.3. Generation of ion's velocity

[Barghouthi *et al.*, 2003 a, b] solved Boltzmann equation in space plasma at high latitudes by using MC method and the relations and expressions we discussed there in this thesis are taken from that paper.

The starting point in the plasma simulations is the injection of an ion into the simulation region, and chosen it with a random initial velocity that corresponds to the distribution function of the ion at the injection point, but at the top of the parosphere (just below the exobase), the ion velocity distribution function was assumed to be non drifting Maxwellian, which can be written as:

$$f(\mathbf{v}) = n\left[\frac{m}{2\pi kT}\right]^{\frac{3}{2}} e^{\frac{-mv^2}{2kT}} \qquad (3.1)$$

Where, $k$ is Boltzmann's constant, $T$ is the temperature at the injected point, $m$ is the mass of the ion, $n$ is the number density, and $v$ is the random velocity of the injected

ion. Which analyzed into two components (parallel velocity and perpendicular velocity) with respect to the geomagnetic field lines, so it is recommended to represent the square of the velocity as: $v^2 = v_{\parallel}{}^2 + v_{\perp}{}^2$, therefore we can rewrite equation (3.1) as:

$$f(\mathbf{v}) = n\left[\frac{m}{2\pi kT}\right]^{\frac{3}{2}} e^{\frac{-m(v_{\parallel}^2 + v_{\perp}^2)}{2kT}} \tag{3.2}$$

and we can rewrite equation (3.2) in more simplest form as:

$$f(\mathbf{v}) = n\left[\left(\frac{m}{2\pi kT}\right)^{\frac{1}{2}} e^{\frac{-mv_{\parallel}^2}{2kT}}\right]\left[\left(\frac{m}{2\pi kT}\right) e^{\frac{-mv_{\perp}^2}{2kT}}\right]$$

$$= nf(v_{\parallel})f(v_{\perp}) \tag{3.3}$$

With:

$$f(v_{\perp}) = \left(\frac{m}{2\pi kT}\right) e^{\frac{-m}{2kT}v_{\perp}^2} \tag{3.4a}$$

$$f(v_{\parallel}) = \left(\frac{m}{2\pi kT}\right)^{\frac{1}{2}} e^{\frac{-m}{2kT}v_{\parallel}^2} \tag{3.3b}$$

Where $f(v_{\perp})$ was the injected ion velocity distribution function which perpendicular to the geomagnetic field lines and $f(v_{\parallel})$ was the injected ion velocity distribution function parallel to the geomagnetic field lines. We will use them to generate $v_{\parallel s}$ and $v_{\perp s}$ velocities of the injected species.

### 3.3.1 Generation of $v_{\perp s}$

Here we need to get random values for random variables of $v_{\perp s}$ at the starting point (injection point) which is distributed over $(0,\infty)$ with probability density equal to one,

$$p(v_{\perp s}) = 2\pi v_{\perp s} f(v_{\perp s}) \tag{3.5}$$

but if we substitute equation (3.2) into equation (3.4), we can get the values of $v_{\perp s}$ are given by:

$$\int_0^{v_{\perp s}} P(v'_{\perp s})\, dv'_{\perp s} = \mathrm{G}' \tag{3.6}$$

where $\mathrm{G}'$ is a random number which taken values between $(0,1)$, we need to find the corresponding value of $v_{\perp s}$, so that we solve equation (3.5) which is shown to be:

$$v_{\perp s}^2 = -\left(\frac{2kT_s}{m_s}\right)\ln(1-\mathrm{G}') \tag{3.7}$$

The above means an ion is injected or initiated with a random $v_{\perp s}$ at the injected point or the exobase.

### 3.3.2 Generation of $v_{\parallel s}$

Now, we must investigate between the local number of ions with $v_{\parallel s}$ and the actual number of those ions which can passed through the lower boundary of the simulation region we chosen it (i.e. those ions $v_{\parallel s} < 0$ will not passed through the assumed injected boundary). The probability of finding an ion passed through the lower boundary is proportional to the ions flux (i.e. the probability of those ions with $v_{\parallel s} < 0$ which they reach or pass through the lower boundary) and is shown below:

$$p(v_{\parallel s}) = p(v_{\parallel s})_{local} \times v_{\parallel s} \times \alpha \tag{3.8}$$

where

$$p(v_{\parallel s})_{local} = f(v_{\parallel s}) = \left[\frac{m_s}{2\pi k T_s}\right]^{\frac{1}{2}} e^{\frac{-m_s}{2kT_s} v_{\parallel s}^2} \tag{3.9}$$

and $\alpha$ is normalizing constant (i.e. $\int_0^{\infty} p(v_{\parallel s})\, dv_{\parallel s} = 1$).

Hence, we obtain the formula that represents the probability density as:

$$p(v_{\parallel s}) = 2\pi v_{\parallel s}\left[\frac{m_s}{2\pi k T_s}\right] e^{\frac{-m_s}{2kT_s} v^2_{\parallel s}} \tag{3.10}$$

Similarly, the values of ion's parallel velocity $v_{\parallel s}$ are given by:

$$v^2_{\parallel s} = -\left(\frac{2kT_s}{m_s}\right)\ln(1-G') \tag{3.11}$$

We want to draw the attention that the formulas for $v_{\perp s}$ and $v_{\parallel s}$ are similar, but they have different numerical values due to $G'$, here we randomly generated an ion from Maxwellian distribution at the boundary level.

## 3.4. The Distribution Function

We discussed in the previous sections that we need in simulation process to inject $10^6$ ions from the injecting point (exobase), these ions will be monitored until they escape from the chosen simulation region which extends from $r = 1.2\, R_e$ to $r = 10\, R_e$, and at each altitude a suitable grid in velocity space is used to register the behavior of these ions, so as to calculate the distribution function.

The time spent by the ion in each pin divided by the bin's volume, was proportional to the ion velocity distribution function at the center of that bin [Barakat and Schunk, 1982c]. But we use the symmetry in azimuthal direction to simplify the registration process, therefore the volume of the bin in velocity space can be represented as $\Delta^3 v = 2\pi v_{\perp} \Delta v_{\parallel}\, \Delta v_{\perp}$ and $f(v) d^3 v$ is equal to the number of the ions with

velocities between $v$ and $v+dv$, however, the time needed for the ion to pass through that bin is:

$$t = \frac{c_1}{\left|v_{\parallel s}\right|}, \tag{3.12}$$

Where $c_1$, was chosen to be arbitrary constant and it represents the width of the bin.

$$\text{but } f_s(v) \ \alpha \ \frac{\frac{c_1}{\left|v_{\parallel s}\right|}}{2\pi v_{\perp s}\Delta v_{\parallel s}\Delta v_{\perp s}}, \tag{3.13}$$

$$\text{so } f_s = \frac{\frac{c_2}{\left|v_{\parallel s}\right|}}{2\pi v_{\perp s}\Delta v_{\parallel s}\Delta v_{\perp s}} \tag{3.14}$$

by letting the width of the bin sides equals to $\frac{1}{3}\left(\frac{2kT_t}{m_t}\right)^{\frac{1}{2}}$ which is (i.e. $\frac{1}{3}$ of the thermal speed of the background ions ), so $\Delta v_{\parallel s} = \Delta v_{\perp s} = \frac{1}{3}\left(\frac{2kT_t}{m_t}\right)^{\frac{1}{2}}$, we must keep in mind that the volume of each bin does not change, but the volume of these bins are different, so this makes that $f_s(v) = \frac{c}{\left|v_{\parallel s}\right|}$, where $c$ is an arbitrary constant.

At each predetermined, so by knowing the parallel $v_{\parallel}$ and the perpendicular $v_{\perp}$ velocities of that ion we can determine the location of it. We use two integers such as $J$ and $I$ to determine the location of the ion where $J = INT(3v_{\perp s})$ and we take in consideration that the distribution is symmetric for $v_{\perp}$ around the geomagnetic field lines (i.e around $v_{\parallel s}$), so $J$ takes the integers from $0$ to $10$, the greatest value for $J$ was chosen to be $10$, because it corresponds to a velocity three times higher than the thermal velocity of the background ions, which is difficult for the test ion to reach. We

insert a restriction $J$ such that $J = Min(J,10)$ to make sure that the sorting is inside the array, in the parallel direction (i.e. the value of $I$ ) we have no azimuthally symmetry so we considered the boundaries of the bins at $(-9.5,-8.5,.....,8.5,9.5)$, where the integer $I$ can be calculated by $I = NINT(3\times v_{\parallel s})$, which take the values between $(-10,10)$, every bin will be known by ($I$ , $J$ and altitude), therefore if the ion crossed a certain bin we can put the numerical value of $f_s(v_s)$ in that bin, after that if another ion crossed the same bin we add its numerical value of $f_s(v_s)$ to the previous one. We kept doing the above procedure until we finished all the ions, so after running the model we get the numerical values for all bins; there for we get the graph for the distribution function of the ions at each altitude by connecting between the bins that have the same numerical values of $f_s(v_s)$.

## 3.5. Moments of the Distribution Function

Here we seek to obtained the moments of the ions (i.e. density $n_i$, drift velocity $u_i$, parallel temperature $T_{\parallel}$ , and perpendicular temperature $T_{\perp}$) at each altitude. The ion distribution function $f_s(v_s)$ is given as, [Barakat and Schunk 1982c]:

$$f(v_s) = 9c_2 \sum_i \frac{1}{\left|v^i_{\parallel s}\right|} \frac{\delta(v_{\parallel s} - v^i_{\parallel s})\delta(v_{\perp s} - v^i_{\perp s})}{2\pi v^i_{\perp s}} \qquad (3.15)$$

Where $\delta(x)$ is the Dirac delta function, and the superscript $i$ denotes that the summation is over all continuous segments of the monitored ion trajectory in the velocity space.

We used the above distribution function to find the expression for the moments in the following sub-sections..

### 3.5.1 The Density

The number density of ions can be written as:

$$n_s = \int f_s(v_s) d^3 v_s = 2\pi \int f_s(v_s) dv_{\parallel s} v_{\perp s} dv_{\perp s}$$

$$= 9c_2 \sum_i 2\pi \int \frac{\delta(v_{\perp s} - v_{\perp s}^i)\delta(v_{\parallel s} - v_{\parallel s}^i) dv_{\parallel s} v_{\perp s} dv_{\perp s}}{2\pi \left| v_{\parallel s}^i \right| v_{\perp s}^i} \tag{3.16}$$

$$n_i = 9c_2 \sum \frac{1}{\left| v_{\parallel s}^i \right|} \tag{3.17}$$

Therefore, after calculating the location of the test ion (i.e. the bin) we add the density store $\frac{1}{\left| v_{\parallel s}^i \right|}$.

### 3.5.2 The Drift Velocity

The drift velocity $u$ of the test ion $s$ is equal to the expectation value of $v_{\parallel s}$ (i.e. $\langle v_{\parallel s} \rangle$):

$$u_s = \frac{\int v_{\parallel s} f_s(v_s) d^3 v_s}{\int f_s(v_s) d^3 v_s} = \frac{\int dv_{\parallel s} v_{\perp s} dv_{\perp s} 2\pi \sum_i \frac{\delta(v_{\perp s} - v_{\perp s}^i)\delta(v_{\parallel s} - v_{\parallel s}^i)}{2\pi \left| v_{\parallel s}^i \right| v_{\perp s}^i}}{\int dv_{\parallel s} v_{\perp s} dv_{\perp s} 2\pi \sum_i \frac{\delta(v_{\perp s} - v_{\perp s}^i)\delta(v_{\parallel s} - v_{\parallel s}^i)}{2\pi \left| v_{\parallel s}^i \right| v_{\perp s}^i}} \tag{3.18}$$

$$u_s = \frac{\sum_i \frac{v_{\parallel s}^i}{\left| v_{\parallel s}^i \right|}}{\sum_i \frac{1}{\left| v_{\parallel s}^i \right|}} = \frac{\sum_i sign(v_{\parallel s}^i)}{\sum_i \frac{1}{\left| v_{\parallel s}^i \right|}} \tag{3.19}$$

Where sign means ( + ) or ( - ).

### 3.5.3 The Perpendicular Temperature

The random thermal velocity is defined as $\mathbf{c_s} = \mathbf{v_s} - \mathbf{u}_s$. From the expectation value for the kinetic energy ($\frac{1}{2}mc_s^2$) we can obtained the thermal energy ($\frac{3}{2}kT_s$) as

$$\frac{3}{2}kT_s = \frac{\int \frac{1}{2}m_s\left[\left(v_{\parallel s} - u_s\right)^2 + v_{\perp s}^2\right]f_s(v_s)d^3v_s}{\int f_s(v_s)d^3v_s} \tag{3.20}$$

$$\frac{1}{2}kT_{\parallel s} + kT_{\perp s} = \frac{\int \frac{1}{2}m_s\left(v_{\parallel s} - u_s\right)^2 f_s(v_s)d^3v_s}{\int f_s(v_s)d^3v_s} + \frac{\int \frac{1}{2}m_s v_{\perp s}^2 f_s(v_s)d^3v_s}{\int f_s(v_s)d^3v_s} \tag{3.21}$$

From equation (3.21) the perpendicular temperature is given by the expectation value of $T_{\perp s} = \frac{1}{k}\left\langle\left(\frac{1}{2}m_s v_{\perp s}^2\right)\right\rangle$, i.e. the second term of equation (3.21), $T_{\perp s}$ is given by:

$$T_{\perp s} = \frac{m_s}{2k}\frac{\sum_i \left(v_{\perp s}^i\right)^2 \Big/ \left|v_{\parallel s}^i\right|}{\sum \frac{1}{\left|v_{\parallel s}^i\right|}} \tag{3.22}$$

We can represented in equation (3.21).

### 3.5.4 The Parallel Temperature

From the equation (3.21), the parallel temperature is represented as:

$$T_{\parallel s} = \frac{\frac{m_s}{k}\int \left(v_{\parallel s} - u_s\right)^2 f_s(v_s)d^3v_s}{\int f_s(v_s)d^3v_s} \tag{3.23}$$

$$T_{\parallel s} = \frac{\frac{m_s}{k}\left[\int v_{\parallel s}^2 f_s(v_s)d^3v_s - 2u_s\int v_{\parallel s} f_s(v_s)d^3v_s + u_s^2\right]}{\int f_s(v_s)d^3v_s} \tag{3.24}$$

and so, it is can be given as:

$$T_{\|s} = \frac{m_s}{k}\left[\frac{\sum_i \left(v_{\|s}^i\right)^2 \Big/ \left|v_{\|s}^i\right|}{\sum_i \frac{1}{\left|v_{\|s}^i\right|}} - \left(\frac{\sum_i sign\left(v_{\|s}^i\right)}{\sum_i \frac{1}{\left|v_{\|s}^i\right|}}\right)^2\right] \tag{3.25}$$

The above MC simulation with the boundary conditions given in Chapter three are used to investigate the effect of wave – particle interactions on $H^+$ and $O^+$ ion outflows in the Auroral regions. For the diffusion coefficient, three different models have been used. The simulation results of these models are compared with the corresponding observations.

# Chapter Four

# The Results

# Chapter Four

# The results

## 4.1. Model I: (The RCC model)

The MC simulation explained in Chapter three was used to simulate the behavior of $H^+$ and $O^+$ ions outflow under the effects of gravitational field, polarization electrostatic field, geomagnetic field, and altitude and velocity dependent wave-particle interactions in the Auroral region. In order to verify our model, we first implemented the simulation for the case of altitude dependent wave-particle interaction (i.e. no velocity dependent wave-particle interactions). The results of this simulation are similar to the results of [Barghouthi, 1997], and these results are presented here for the sake of comparison between the effects of altitude dependent WPI and altitude and velocity dependent WPI, in order to understand the effect of velocity dependent WPI on the ion outflows and the importance of this effect.

### 4.1.1 $H^+$ ions

The ion velocity distributions for $H^+$ ions at different altitudes are presented in Figure 4.1. The left panel of Figure 4.1 shows the effect of altitude dependent WPI, at the injection point, 1.2 $R_E$, the ion velocity distribution is consistent with the boundary conditions, i.e. $f(H^+)$ is drifting Maxwellian. However, as altitude increases, the distribution function develops conic features and these features saturate at higher altitudes. The formation of ion conic is due to the combined effects of wave-particle interactions, which heats the ions in the perpendicular direction, and to the mirror force,

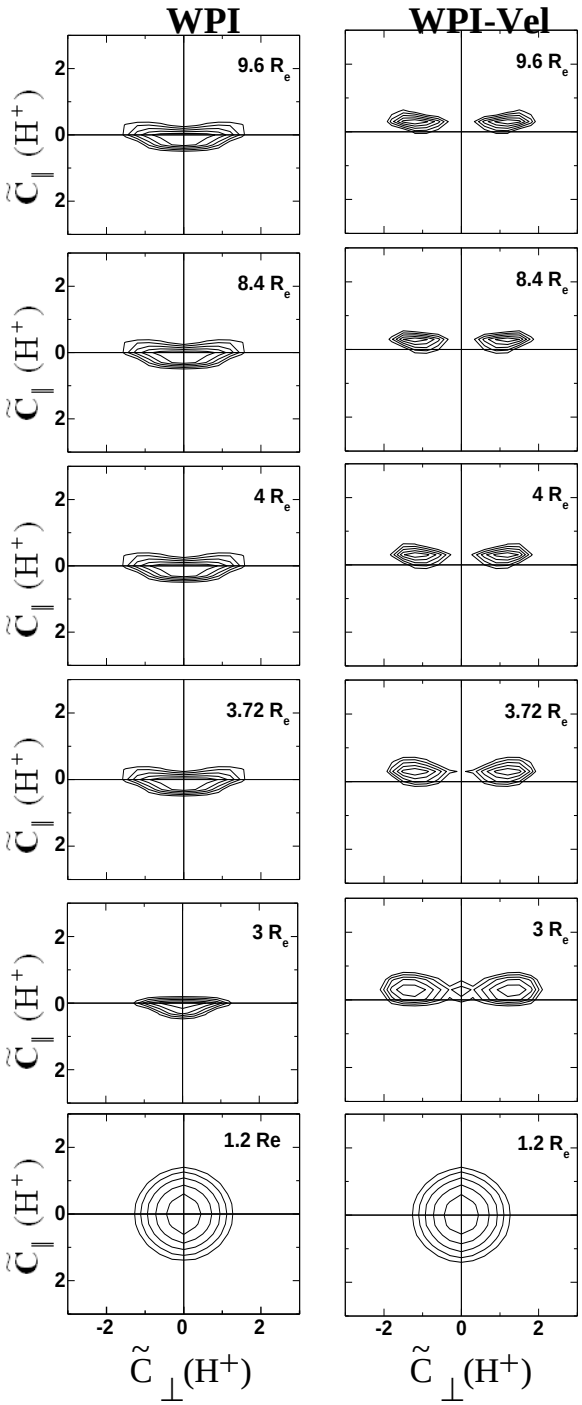


**Figure 4.1:** $H^+$ velocity distributions for the case of WPI (left panel) and for WPI-velocity dependent diffusion coefficient (right panel) at different geocentric altitudes. $f(H^+)$ is represented by equal-value contours in the normalized velocity ($\tilde{C}_{\parallel}, \tilde{C}_{\perp}$) plane, where $\tilde{\mathbf{c}} = \left[\mathbf{v} - \mathbf{u}(H^+)\right] / \left[2kT(H^+)/m(H^+)\right]^{1/2}$ The contour levels decrease successively by a factor $e^{1/2}$ from the maximum.

which converts some of the energy gained in the perpendicular direction over to the parallel direction. The right panel of Figure 4.1 shows the effect of altitudes and velocity dependent wave-particle interactions. At the injection point, the $H^+$ distribution function is drifting Maxwellian, however, as altitude increases, the distribution function develops toroidal features, and these features saturate at higher altitudes.

The peaked nature of the diffusion coefficient $D_\perp$ (Equation. (2.25)) reflects the way in which wave-particle interactions lead to the formation of ion toroids. Because $D_\perp$ falls to zero at small perpendicular velocities ($i.e\, v_\perp << v_\circ$), the bulk of the ion velocity distribution is unaffected by interaction with the waves (electromagnetic turbulence). As $v_\perp$ increases and becomes near $v_\circ$, $D_\perp$ begins to become appreciable and very significant, respectively, and the diffusion process begins to affect the $H^+$ ions in the distribution by heating them in the perpendicular direction. Above the peak, when $v_\perp >> v_\circ$, the diffusion coefficient $D_\perp$ decreases very rapidly as $(v_\perp / v_\circ)^{-3}$ and consequently, the effect of wave–particle interactions becomes negligible. Because there are initially more ions at lower velocities than at higher velocities, the net escape flux in velocity space is toward higher velocities, leading to the formation of toroids. In other words, the ions tend to move out of the region of large diffusion ( $v_\perp \approx v_\circ$) and accumulate in the region of relatively low $D_\perp$ ( $v_\perp >> v_\circ$) forming the aforementioned toroidal ion velocity distributions "Donuts". Also, as altitude increases the ion velocity distribution saturates, because most of the ions in the bulk of the distribution moved out to the region of low $D_\perp$. In that region the effect of WPI is negligible, and the ions drift upward under the effect of body forces and diverging of geomagnetic field. In other words, the heated $H^+$ ions drift upward along the geomagnetic field lines; they eventually leave the primary heating region, thus, the heating process turned to be self-

limiting [Barghouthi and Atout, 2006]. This scenario may explain the saturation of the toroidal ion velocity distribution. Therefore, including the effect of velocity dependent wave-particle interactions (right panel of Figure 4.1) produce the toroidal $H^+$ ion velocity distributions, and this is due to the peaked nature of $D_\perp$.

Figure 4.2 shows the profiles of $H^+$ density n($H^+$), drift velocity u($H^+$), parallel temperature $T_\parallel(H^+)$ and perpendicular temperature $T_\perp(H^+)$, for two cases, altitude dependent and velocity independent WPI (solid) and altitude and velocity dependent WPI (dotted). Including the velocity dependent WPI decreases the drift velocity u($H^+$) (top right panel), because as altitude increases most of the ions move out to a region of negligible WPI, and this decreases the upward mirror force, and, hence the acceleration in the upward direction is decreased. Since the $H^+$ ions are in flux-limiting flow condition a corresponding increase in the $H^+$ density n($H^+$) (top left panel) is expected to compensate for the decrease in u($H^+$), thereby keeping the net escape flux constant. The behavior of perpendicular temperature $T_\perp(H^+)$ (bottom left panel) is a result of the competition between the heating process due to WPI and perpendicular adiabatic cooling. For the case of altitude dependent WPI (solid), the transverse heating due to WPI dominates the perpendicular adiabatic cooling at most altitudes, only at very low altitudes, the perpendicular cooling dominates the perpendicular heating. However, including the effect of velocity dependent WPI (dotted) decreases the heating in the perpendicular direction, but still, the heating process, slightly, overcomes the perpendicular adiabatic cooling.

The profiles of $H^+$ parallel temperatures $T_\parallel(H^+)$ are presented in Figure 4.2 (bottom left panel). The behavior of $T_\parallel(H^+)$ is a result of the balance between two effects. firstly, the perpendicular heating increases the upward mirror force, and

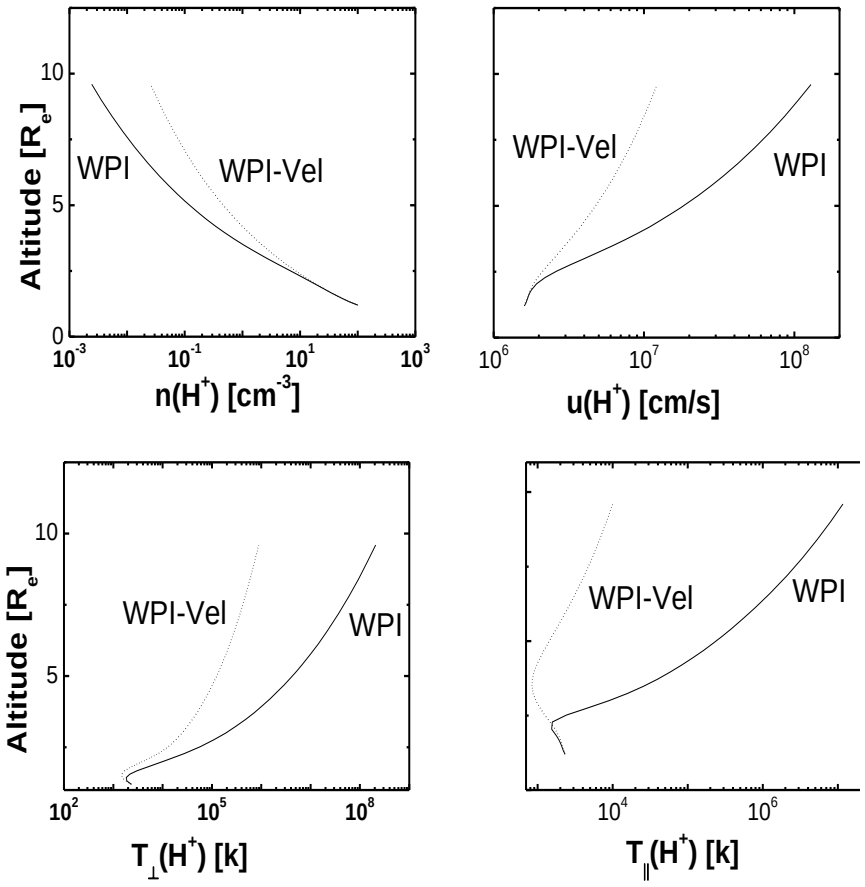


**Figure 4.2:** Altitude profiles of the lower order $H^+$ moments for the case of WPI-velocity dependent (dotted) and WPI (solid). The moments considered here are density $n(H^+)$ (top left), drift velocity $u(H^+)$ (top right), perpendicular temperature $T_\perp(H^+)$ (bottom left), and parallel temperature $T_\parallel(H^+)$ (bottom right).

consequently, the parallel adiabatic cooling is strengthened [Barghouthi *et al.*, 1998]. secondly, as the ions drift upward along diverging geomagnetic field lines, $T_\parallel(H^+)$ increases due to the energy transfer from perpendicular direction over to the parallel direction. The parallel adiabatic cooling dominates for altitudes below 3 $R_E$ and 4 $R_E$, for the case of altitude dependent WPI and for the case of altitude and velocity dependent WPI, respectively. Including the effect of velocity dependent WPI decreases the energy transfer from perpendicular direction over to the parallel direction.

### 4.1.2 $O^+$ ions

Similarly, Figsures 4.3 and 4.4 present the $O^+$ ions velocity distributions and $O^+$ moments, respectively, for two cases, altitude dependent and velocity independent WPI, and altitude and velocity dependent WPI. The left panel of Figure 4.3 shows the effect of altitude dependent and velocity independent WPI on $O^+$ ions velocity distribution. At the injection point, $f(O^+)$ is Maxwellian and consistent with the assumed boundary conditions. However, as altitude increases $f(O^+)$ develops conic distributions, because geomagnetic field strength decreases with altitude, thus the adiabatic motion of the $O^+$ ions drifting to higher altitudes transforms the heated distribution into one that is more geomagnetic field aligned, i.e., a conic [Chang, 1993]. The right panel of Figure 4.3 presents the effect of including the velocity dependent WPI on $O^+$ ions velocity distribution. At the injection point, 1.2 $R_E$, $f(O^+)$ is Maxwellian, and as altitude increases $f(O^+)$ develops into a toroidal distribution, and this distribution saturates at higher altitudes, due to the self-limiting heating process explained above. Also, this is due to the peaked nature of the perpendicular diffusion coefficient $D_\perp$ given by equation (2.26), in which $D_\perp$ is negligible for $v_\perp << v_\circ$ and consequently, the effect of WPI is not dominant, and when $v_\perp$ becomes around $v_\circ$, the diffusion coefficient becomes maximum and the effect of WPI turns to be very important and crucial, but again, for $v_\perp >> v_\circ$, the effect of WPI becomes negligible and decreases, rapidly, as $(v_\perp / v_\circ)^{-3}$. This behavior of $D_\perp$ and hence, of altitude and velocity dependent WPI affects the $O^+$ ions and kicks it out of the heating zone into a region of negligible heating forming the toroidal distribution in the velocity space. Therefore, including the effect of velocity dependent WPI produces the $O^+$ and $H^+$ toroids at altitudes above ~ 3

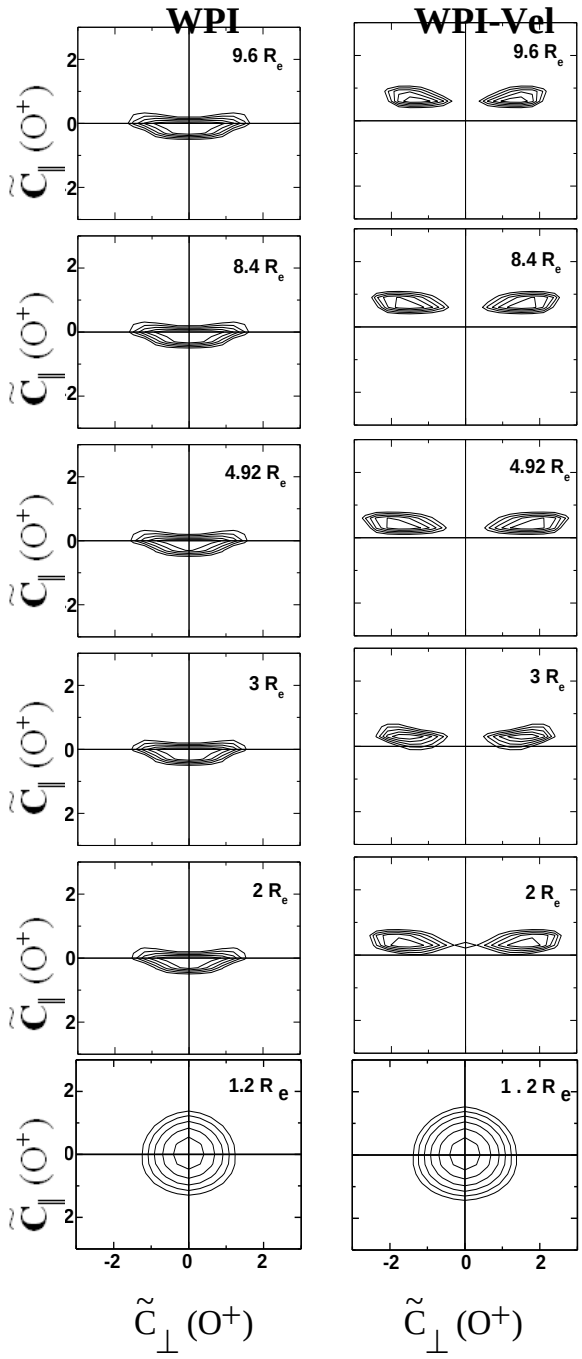


**Figure 4.3:** $O^+$ Velocity distributions for altitude dependent and velocity independent WPI (left panel) and for altitude and velocity dependent WPI (right panel), at different geocentric altitudes. $f(O^+)$ is represented by equal-value contours in the normalized velocity ($\tilde{C}_{\parallel}$, $\tilde{C}_{\perp}$) plane, where $\tilde{\mathbf{c}} = \left[\mathbf{v} - \mathbf{u}(O^+)\right] / \left[2kT(O^+)/m(O^+)\right]^{1/2}$ The contour levels decrease successively by a factor $e^{1/2}$ from the maximum.

$R_E$. However it did not produce the $O^+$ ions conics at low altitudes (~ 2 $R_E$) which have been observed [Winningham and Burch, 1984, Crew *et al*., 1990].

Figure 4.4, shows the $O^+$ ions velocity moments in the Auroral region for two cases, altitude dependent WPI (solid) and altitude and velocity dependent WPI (dotted). The drift velocity (solid), u($O^+$), increases with altitude, because $D_\perp(O^+)$, equation (2.23), increases, monotonically, with altitude and hence, WPI heats the $O^+$ ions in the perpendicular direction at all altitudes and due to the mirror force the $O^+$ ions accelerate into the upward direction. However, including the effect of velocity dependent WPI decreases the heating rate in the perpendicular direction, due to the variation of $D_\perp(O^+)$ with altitude and perpendicular velocity, and this decreases the effect of mirror force which leads to the decreasing of the ion's acceleration in the upward direction. Therefore, including the effect of velocity dependent WPI decreases the drift velocity (dotted), u ($O^+$), as shown in the top left panel of Figure 4.4. As mentioned before, and for the case of velocity dependent WPI, since $O^+$ ions are in the flux-limiting flow condition, a corresponding increase in the ions density (top left panel) is expected in order to compensate for the decrease in the ions drift velocity ,and hence, to keep the net escape flux constant. The behavior of $O^+$ ion's perpendicular temperature $T_\perp(O^+)$ (bottom left panel, dotted) decreases very rapidly as a result of including the effect of velocity dependent WPI, because the heating in the perpendicular direction decreases as a result of the variation behavior of $D_\perp(O^+)$ (equation (2.26)). The energy transfer from perpendicular direction over to the parallel direction due to the mirror force decreases, because the heating in the perpendicular direction is decreased as a result of including velocity dependent WPI, this explains the behavior of $T_\parallel(O^+)$ (bottom left panel, dotted) as shown in Figure 4.4.

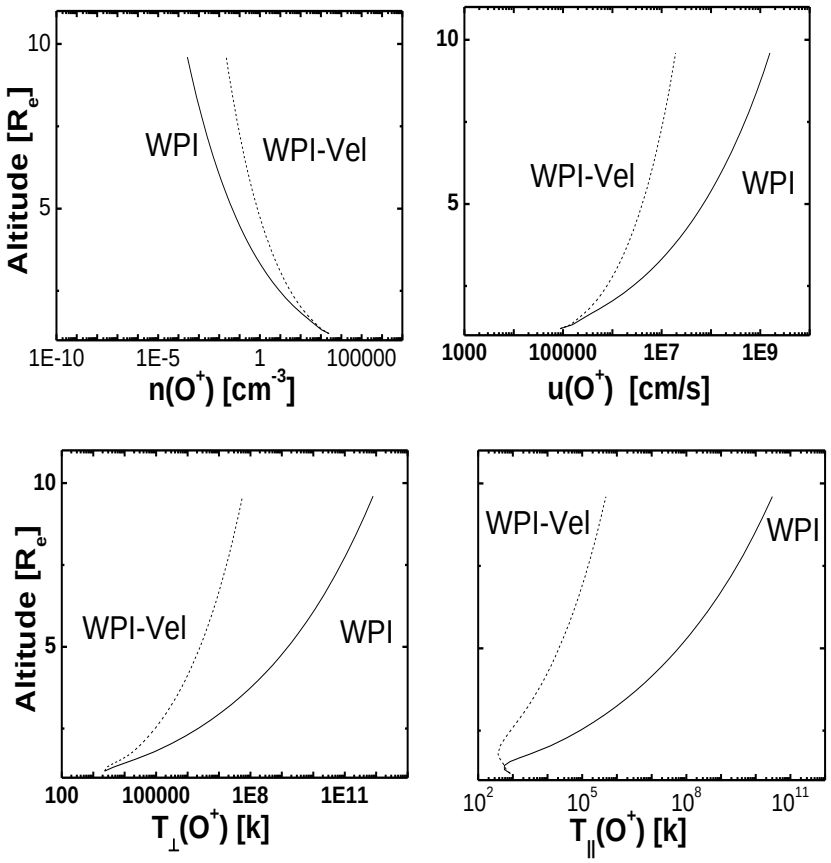


**Figure 4.4:** Altitude profiles of the lower order $O^+$ moments for the case of altitude and velocity dependent WPI (dotted) and for the case altitude dependent and velocity independent WPI (solid). The moments considered here are density $n(O^+)$ (top left), drift velocity $u(O^+)$ (top right), perpendicular temperature $T_\perp(O^+)$ (bottom left), and parallel temperature $T_\parallel(O^+)$ (bottom right).

In general, as a result of perpendicular heating due to altitude dependent and velocity independent WPI, the $H^+$ and $O^+$ ion velocity distribution develop a conic shape at altitudes greater than 2 $R_E$, and the ion temperature tends to be more sensitive to the influence of altitude dependent WPI than the lower order moments. This should be expected since the direct effect of the WPI is to heat the ions in the perpendicular direction. In contrast, the ion densities and drift velocities are affected indirectly through enhanced mirror force. To be specific, the adoption of this model of altitude dependent and velocity independent WPI, and similar ones such as that adopted by

[Crew *et al*., 1990] produces unrealistically high $H^+$ and $O^+$ ions temperatures at altitudes of several $R_E$. However, including the effect of velocity dependent WPI produces $O^+$ and $H^+$ toroids at altitudes greater than 3 $R_E$, and decreases the $H^+$ and $O^+$ ions temperatures to be realistic and comparable to observations of [Huddleston *et al*., 2000].

[Huddleston *et al*., 2000] reported the observations of $H^+$ and $O^+$ toroids, T ($O^+$) = 200 eV, and T ($H^+$) = 78 eV at 4.8 $R_E$ in the equatorward of the cusp. The above MC model (velocity and altitude dependent WPI ) produces $H^+$ and $O^+$ toroids at high altitudes, as shown in the right panels of Figures 4.1 and 4.3, respectively, and this is consistent with above observations. However, for $H^+$ and $O^+$ ions temperatures, the MC model produces T ($O^+$) = 115 eV, and T ($H^+$) = 6 eV at 4.8 $R_E$, these simulation results are very far from the above observed values. Also, the above model (velocity and altitude dependent WPI) did not produce the observed $O^+$ ions conic distributions at 2 $R_E$ [Winningham and Burch, 1984; Crew *et al*., 1990]. However, it produced the $O^+$ ion conics at 2 $R_E$ when the effect of velocity dependent WPI was not included as shown in the left panel of Figure 4.3. Therefore, we conclude the current model produces acceptable results for $H^+$ and $O^+$ ions distributions at high altitudes (i.e. toroids); however, at low altitudes the simulation results of $O^+$ ions velocity distributions are inconsistent with observations. According to $H^+$ and $O^+$ ions temperatures, the model produces values that are inconsistent with observations, but they are closer to the observed values more than the values obtained when the effect of velocity dependent WPI was not included (e.g. T ($O^+$) = 5.8 x $10^4$ eV, and T ($H^+$) = 177.4 eV at 4.8 $R_E$ ). Therefore, we said that the model produced unrealistic values of ions temperatures when the effect of velocity dependent WPI was not included, and produce realistic values after its inclusion.

## 4.2. Model II: (The Bouhram Model)

The Bouhram model is used to calculate the $O^+$ and $H^+$ ions velocity distributions $f_i$ and the following lower order velocity moments:

$$n_i = \int f_i d^3 v_i \tag{4.1}$$

$$u_i = \frac{1}{n_i} \int v_{i\parallel} \; f_i d^3 v_i \tag{4.2}$$

$$T_{i\parallel} = \frac{m_i}{n_i k} \int \left( v_{i\parallel} - u_i \right)^2 f_i d^3 v_i \tag{4.3}$$

$$T_{i\perp} = \frac{m_i}{2 n_i k} \int v_{i\perp}{}^2 f_i d^3 v_i \tag{4.4}$$

in above equations i denotes the type of the ions ($O^+$ or $H^+$), $n_i$, $u_i$, $T_{i\parallel}$, and $T_{i\perp}$ are the ion density, drift velocity, parallel temperature, and perpendicular temperature.

Figure 4.5 shows the $O^+$ velocity distribution $f(O^+)$ at different altitudes and for different values of electromagnetic turbulence wave length $\lambda_\perp$. For the case of $\lambda_\perp = \infty$ (i.e. the velocity dependence of $D_\perp$ was not taken into consideration) the results are consistent with those of [Bargouthi, 1997], at 1.2 $R_E$ $f(O^+)$ is consistent with boundary conditions, and as altitude increases, the distribution function develops conic features at 1.8 $R_E$ and above. The formation of the conic is due to altitude dependent WPI, which heats the ions in the perpendicular direction, and to the mirror force, which converts some of the energy gained in the perpendicular direction over to the parallel direction. At higher altitudes, the ion velocity distribution $f(O^+)$ saturates owing to dominant WPI. Also, as mentioned before for small infinite wave length limit, $k_{\perp\circ} \rho_i << 1, J_\circ \sim 1$,

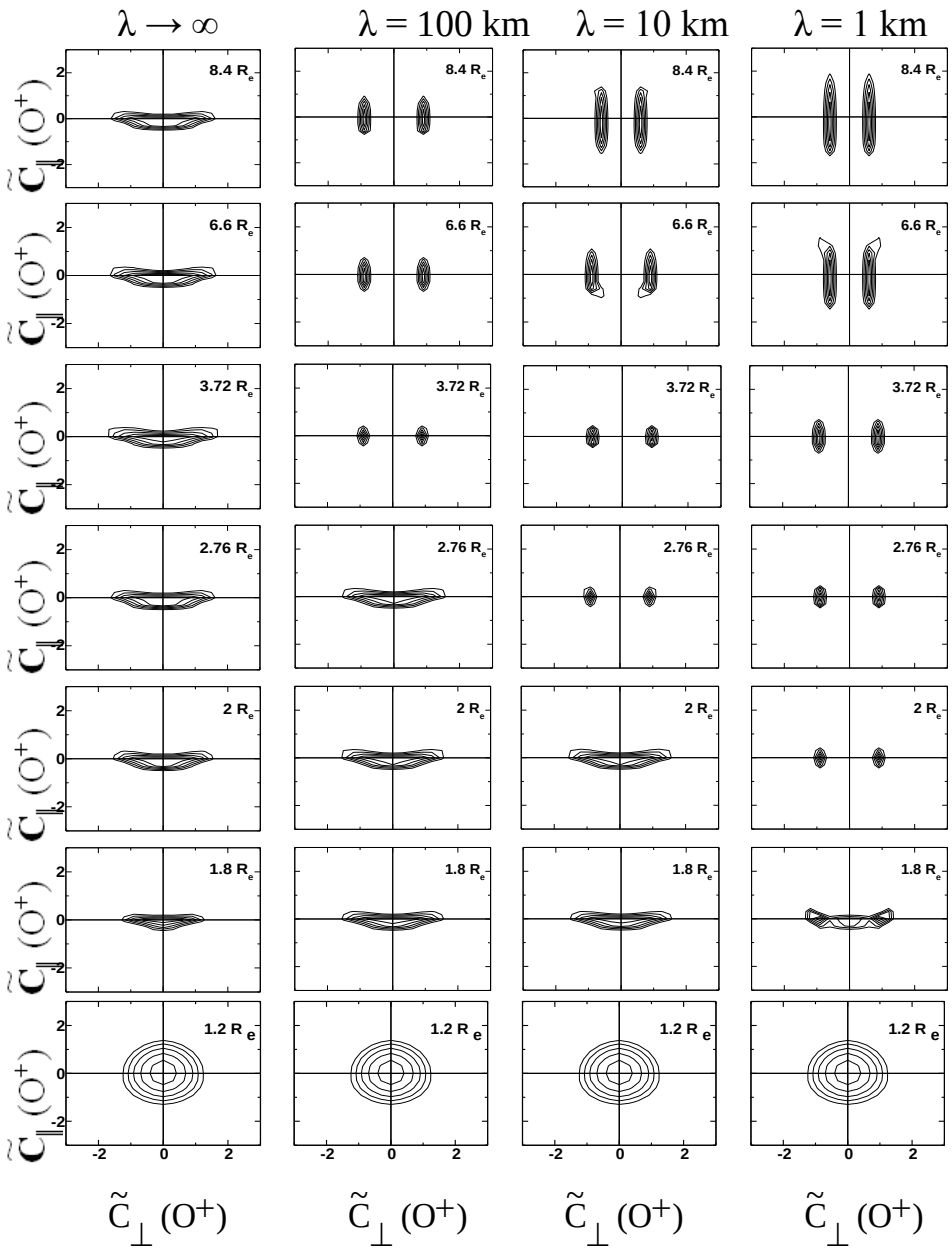


**Figure 4.5:** $O^+$ ions velocity distribution functions at different geocentric distances (1.2, 2.0, 2.76, 3.0, 4.4, 6.6, and 7.2 $R_e$) for different electromagnetic turbulence wavelengths ($\lambda_\perp$), the wavelengths considered here are $\lambda_\perp \to \infty$ (1st panel). $\lambda_\perp = 100\ km$ (2nd panel). $\lambda_\perp = 10\ km$ (3rd panel) $\lambda_\perp = 1\ km$ (4th panel). $f\left(O^+\right)$ is represented by equal values contours in the normalized velocity ($\tilde{c}_\parallel$ ,$\tilde{c}_\perp$) plane, where $\tilde{\mathbf{c}} = \left[\mathbf{v} - \mathbf{u}(O^+)\right] / \left[2kT(O^+)/m(O^+)\right]^{1/2}$. The contour levels decrease successively by a factor $e^{1/2}$ from the maximum.

i.e., the heating rate is independent of the ion velocity. For the case of $\lambda_\perp$ = 100 Km, the $f(O^+)$ is similar to the case of $\lambda_\perp = \infty$ up to ~ 2.76 $R_E$. at altitude (~3.72 $R_E$) the distribution function displace toroidal features. This toroidal shape can be explained if we remember that $D_\perp$ (equation (2.28)) peaks near $v_\perp \cong 0$ and decreases very rapidly, as $J^2_\circ\left(\frac{k_\perp v_\perp}{\Omega_i}\right)$, for large values of $v_\perp$; therefore, the ions tend to move out of the region of large diffusion and accumulate in the region of relatively low $D_\perp$, forming the aforementioned toroidal distributions. At very high altitude (~6.6 $R_E$ and above), the heating rate becomes negligible, and the effect of wave-particle interaction turns to be not significant. In the absence of wave-particle interactions, ions move under the effect of body forces (i.e. due to gravitational and polarization fields) and the mirror force due to the divergence of geomagnetic field, and the ion motion can be described by Liouville theorem [Barakat and Schunk, 1983]. At these high altitudes, $f(O^+)$ develops temperature anisotropy, and an asymmetry with an upward tail. The anisotropy is due to perpendicular adiabatic cooling, which occurs as $O^+$ ions drift upward into regions of lower magnetic field the perpendicular temperature decreases in order to kept the conservation of the first adiabatic invariant ($\eta$). This explains the behavior of $O^+$ ions at 6.6 $R_E$ and 8.4 $R_E$ altitudes for the case of $\lambda_\perp$ = 100 Km. As $\lambda_\perp$ decreases, the toroidal features appear at lower altitudes, at 2.76 $R_E$ and 2 $R_E$ for $\lambda_\perp$ = 10 Km and 1 Km, respectively, also above these altitudes the effect of wave-particle interactions becomes negligible and the motion of $O^+$ ions is described by Liouville theorem as shown above. As $\lambda_\perp$ decreases, the argument of Bessel function, $\left(\frac{2\pi v_\perp}{\lambda_{\perp\circ}\Omega_i}\right)$, increases and

consequently, $J_\circ$ decreases and then the heating rate becomes negligible and the effect of WPI turns to be not important.

The effect of altitude and velocity dependent wave-particle interactions on the $O^+$ low-order velocity moments is presented in Figure 4.6. Altitude profiles for ion density n($O^+$), drift velocity u($O^+$), parallel temperature $T_\parallel$ ( $O^+$), and perpendicular temperature $T_\perp$( $O^+$) are given for $\lambda_\perp = \infty$ (solid), $\lambda_\perp$ = 100 Km (dashed), $\lambda_\perp$ = 10 Km (dotted), and $\lambda_\perp$ = 1 Km (dotted dashed). The top right panel of Figure 4.6 shows the profiles of u($O^+$) for different values of $\lambda_\perp$. At low altitudes, the argument $k_{\perp\circ}\rho_i$ is much less than unity, and hence the profiles of u($O^+$) coincide for all values of $\lambda_\perp$, i.e., the effect of velocity dependent wave-particle interaction is negligible because $J_\circ \sim 1$. For the case $\lambda_\perp$ = 100 Km, the heating (accelerating) rate and hence u($O^+$) is reduced above a saturation level of about 3 $R_E$, in comparison to the case of ( $\lambda_\perp = \infty$). This is an obvious result of the heating process because the heating rate decreases when $k_{\perp\circ}\rho_i > 1$. As $\lambda_\perp$ decreases, $k_{\perp\circ}\rho_i$ becomes greater than unity at lower altitudes and consequently the saturation level occurs at lower altitudes. Above the saturation level, the drift velocity is almost constant and this is due to the conservation of energy because there is no heating and the motion is under the effect of body and mirror forces. Therefore, as $\lambda_\perp$ decreases, the drift velocity decreases because of the reduction of the heating rate, and $O^+$ density n($O^+$) (top left panel) increases to keep the escape flux constant [Barghouthi *et al.*, 1998]. The $O^+$ perpendicular temperature (bottom-left panel) monotonically increases for the case of $\lambda_\perp = \infty$, and the model produce unrealistic temperatures at high altitudes (~ $10^{11}$ Km )and this is due to the heating in the perpendicular direction due to altitude dependent and velocity independent wave-particle interaction. However, including the effect of velocity dependent wave-particle

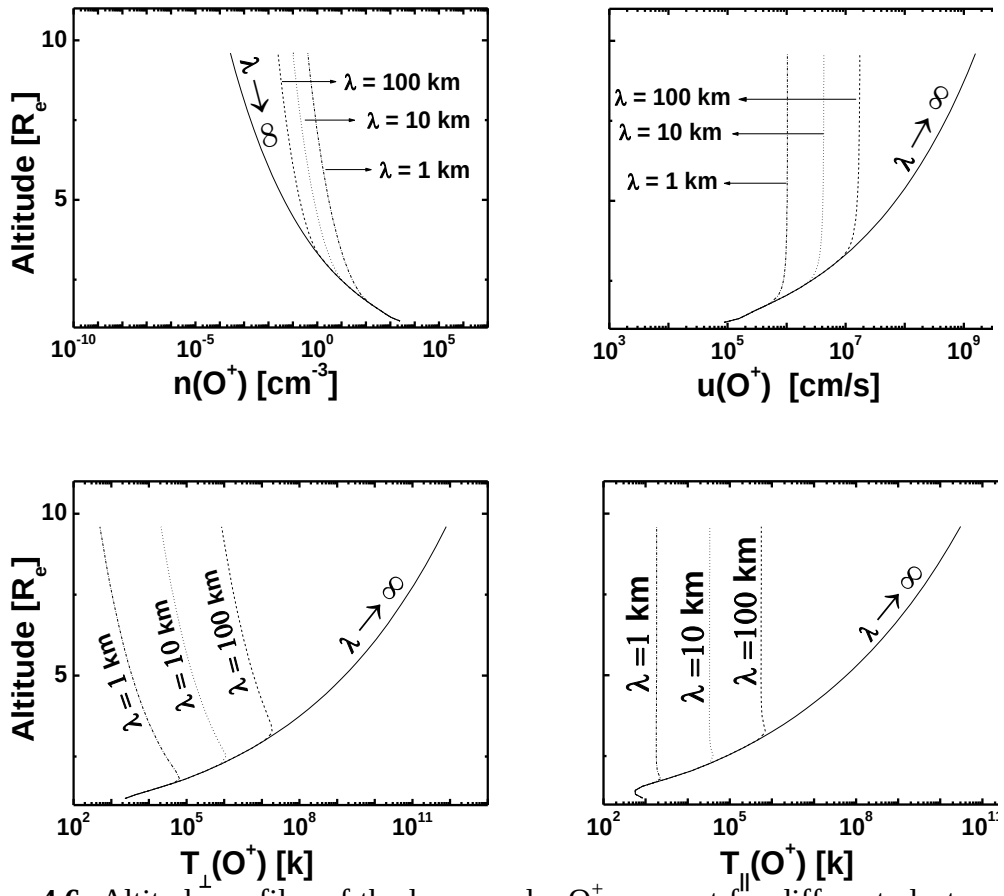


**Figure 4.6:** Altitude profiles of the lower order $O^+$ moment for different electromagnetic turbulence wavelengths ($\lambda_\perp$). The wavelengths considered here are $\lambda_\perp \to \infty$ (solid), $\lambda_\perp = 100\ km$ (dashed), $\lambda_\perp = 10\ km$ (dotted), $\lambda_\perp = 1\ km$ (dashed dotted). The $O^+$ moments considered here are: density $n(O^+)$ (top left), drift velocity $u(O^+)$ (top right), perpendicular temperature $T_\perp(O^+)$ (bottom left), and parallel temperature $T_\parallel(O^+)$ (bottom right).

interaction reduces $T_\perp(O^+)$, especially at high altitude, to a realistic temperatures. This reduction is expected because as $\lambda_\perp$ decreases, $k_\perp \rho_i$ becomes greater than unity and the heating rate turns to be negligible. The behavior of $T_\perp(O^+)$ above the saturation level is consistent with the features of the $O^+$ velocity distribution presented in Figure 4.5. In the absence of wave-particle interaction, i.e. above the saturation level, the motion of $O^+$ ions

under the effect of body and mirror forces and consequently, energy transferred from perpendicular direction to the parallel direction in order to keep ($\eta$) constant. The wave-particle interaction can influence the behavior of $O^+$ parallel temperature $T_\parallel$ ($O^+$) in two indirect ways [Barakat and Barghouthi, 1994 (a, b)]. First the increased upward mirror force enhances the parallel adiabatic cooling. Second, the transfer of the energy from the perpendicular direction to the parallel direction tends to enhance $T_\parallel$ ($O^+$). The balance between these two effects determines the behavior of $T_\parallel$ ($O^+$). Similarly, Figure 4.7 present the effect of altitude and velocity dependent wave-particle interaction, on $H^+$ ion velocity distributions for different values of $\lambda_\perp$ and at different altitudes. At the exobase $f(H^+)$ is consistent with boundary conditions, and bi-Maxwellian at 2 $R_E$ for all $\lambda_\perp's$ due to perpendicular heating. The conic features appear at 2.76 $R_E$ and saturated for $\lambda_\perp = \infty$, however toroidal features appear at 6.6 $R_E$, 4.4 $R_E$, and 3 $R_E$, for $\lambda_\perp$ = 100 Km, 10 Km, and 1 Km, respectively. The behavior of $f(H^+)$ at high altitudes for the case of $\lambda_\perp$ = 1Km, can be described in terms of Liouville theorem noted earliar. The difference between the behavior of $O^+$ and $H^+$ under the influence of altitude and velocity dependent wave-particle interactions is due to two factors. First, the large mass ratio($m_{O+}=16m_{H+}$) and secondly, the preferential heating of $O^+$ due to pressure cooker effect [Barakat and Barghouthi, 1994a]. The heating rate is significant for $k_{\perp\circ}\rho_i \geq 1$ consequently, the saturation point occurs at higher altitudes for $H^+$ than for $O^+$. Figure 4.8 shows the profiles of the lower order moment for $H^+$ ions. The behavior of $H^+$ ions below the saturation point (i.e., $k_{\perp\circ}\rho_i < 1$ ) is the same for all values of $\lambda_\perp$ because $J_\circ \sim 1$. Above, the saturation point the $H^+$ moments display trends similar to those of $O^+$ moments as $\lambda_\perp$ decreases. For example, the drift velocity u($H^+$) (top-right panel) decreases due to the

reduction in the heating rate and consequently, the density n($H^+$) (top left panel) increases to keep the net escape flux constant. Because of the significant reduction in the heating rate above the saturation point, $H^+$ perpendicular temperature (bottom left panel) decreases in order to keep the first adiabatic invariant $\eta$ constant, and consequently $T_{\parallel}$ ($O^+$) (bottom right panel) decreases as $\lambda_{\perp}$ decreases. In an on going study, a comparison has been made between the above results and the results of other model with observations at high altitudes and high-latitudes. Qualitatively, the results of this model are comparable to the observations.

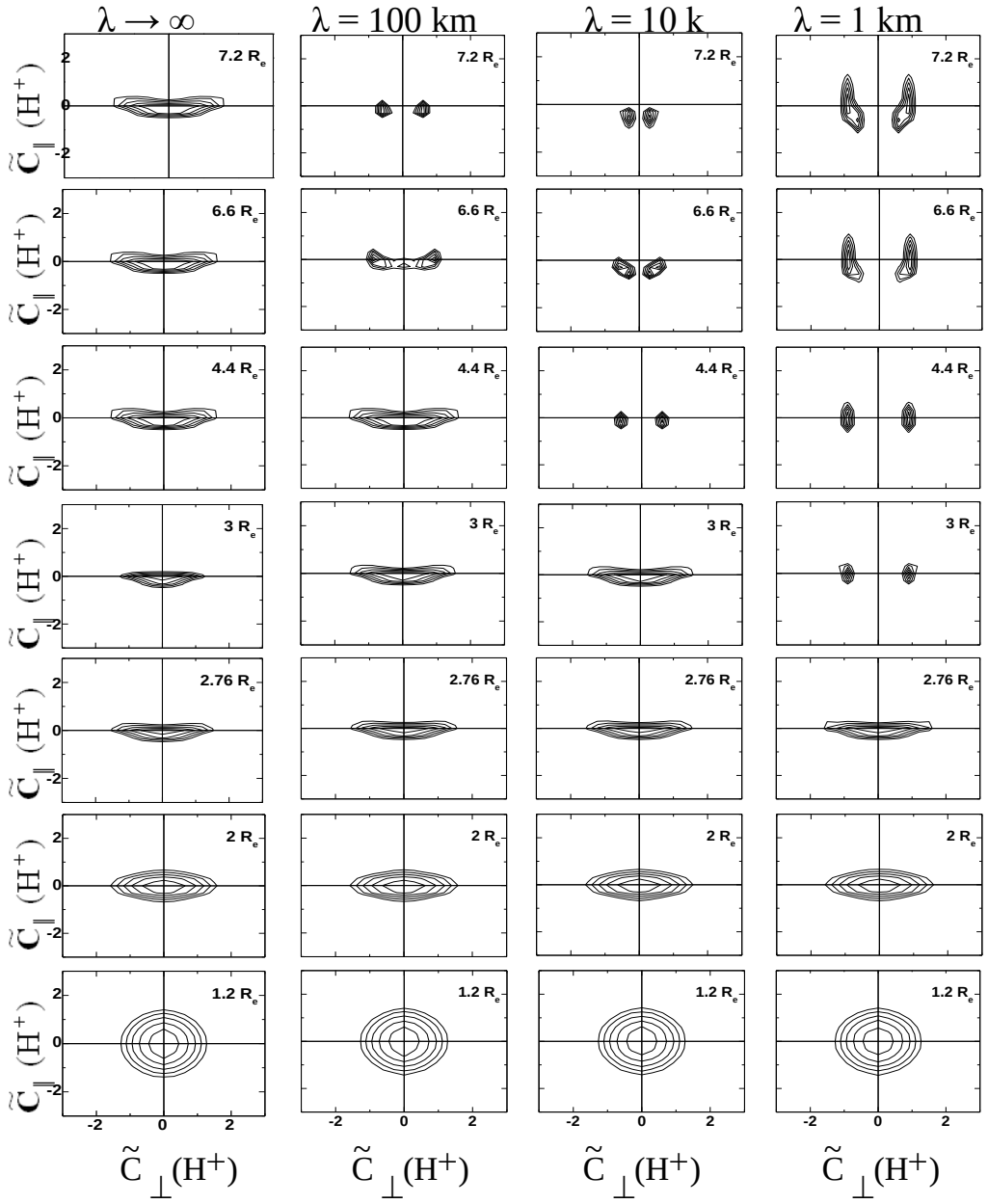


**Figure 4.7:** $H^+$ ions velocity distribution functions at different geocentric altitudes (1.2, 2.0, 2.76, 3.0, 4.4, 6.6, and 7.2 $R_e$) for different electromagnetic turbulence wavelengths ($\lambda_\perp$), the wavelengths considered here are $\lambda_\perp \to \infty$ (1st panel), $\lambda_\perp = 100\ km$ (2nd panel). $\lambda_\perp = 10\ km$ (3rd panel), and $\lambda_\perp = 1\ km$ (4th panel). $f\left(\mathrm{H}^+\right)$ is represented by equal values contours in the normalized velocity $(\tilde{c}_\parallel, \tilde{c}_\perp)$ plane, where $\tilde{\mathbf{c}} = \left[\mathbf{v} - \mathbf{u}(\mathrm{H}^+)\right] / \left[2kT\left(\mathrm{H}^+\right)/m\left(\mathrm{H}^+\right)\right]^{1/2}$. The contour levels decrease successively by a factor $e^{1/2}$ from the maximum.

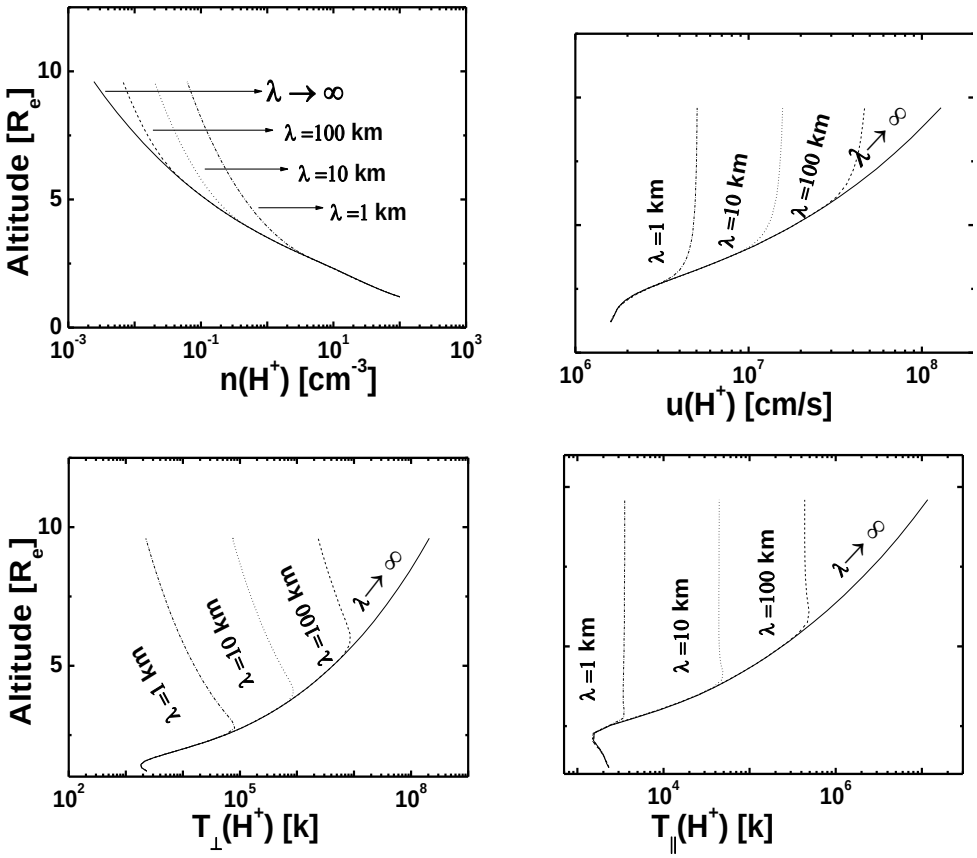


**Figure 4.8:** Altitude profiles of the lower order $H^+$ moment for different electromagnetic turbulence wavelengths ($\lambda_\perp$). The wavelengths considered here are $\lambda_\perp \to \infty$ (solid), $\lambda_\perp = 100\ km$ (dashed). $\lambda_\perp = 10\ km$ (dotted) $\lambda_\perp = 1\ km$ (dashed dotted). The $H^+$ moments considered here are: density $n(H^+)$ (top left), drift velocity $u(H^+)$ (top right), perpendicular temperature $T_\perp(H^+)$ (bottom left), and parallel temperature $T_\parallel(H^+)$ (bottom right).

## 4.3. Model III: (The Barghouthi Model)

For the sake of comparison between the RCC and the Bouhram models, we shall reproduce the results of [Barghouthi and Atout, 2006].

### 4.3.1 $H^+$ ions

Because there is no information about the wavelength of the electromagnetic turbulence ($\lambda_\perp$), they have chosen a wide range ($\lambda_\perp = 1\,Km$, $\lambda_\perp = 10\,Km$, and $\lambda_\perp = 100\,Km$) that covers the circumstances expected to occur in the Auroral region. Figure 4.9 shows the $H^+$ ions velocity distribution function $f(H^+)$ at different altitudes extended from ($1.2\,R_E$ to $9.6\,R_E$) and for different values of $\lambda_\perp$ which are ($\lambda \to \infty$,100 Km ,10 Km ,and 1 Km). For the case ($\lambda \to \infty$), i.e. the effect of finite Larmor radius is negligible, they have reproduced the results of [Barghouthi, 1997] and at ($1.2R_E$) in the first panel we see the maxwellian feature. We also see that for the case ($\lambda_\perp = 100\,Km$) the distribution function remains the same as the case ($\lambda \to \infty$) up to $4.9\,R_E$ ( 1st and 2nd panels ), but at high altitudes ($\sim 7.2R_E$) the distribution function displays toroidal features, and this toroidal shape can be explained since ($D_\perp$) peaks near ($v_\perp = 0$), and decreases rapidly for large values of ($v_\perp$); therefore, the ions tend to move out of the region of large diffusion ($v_\perp \cong 0$) and accumulate in the region of relatively low ($D_\perp$) forming the aforementioned toroidal distribution function. This mechanism [Barghouthi and Atout, 2006] successfully in explained the toroidal shape of distribution function observed by [Huddleston *et al.*, (2000)] as mentioned in Barghouthi, 2003a.

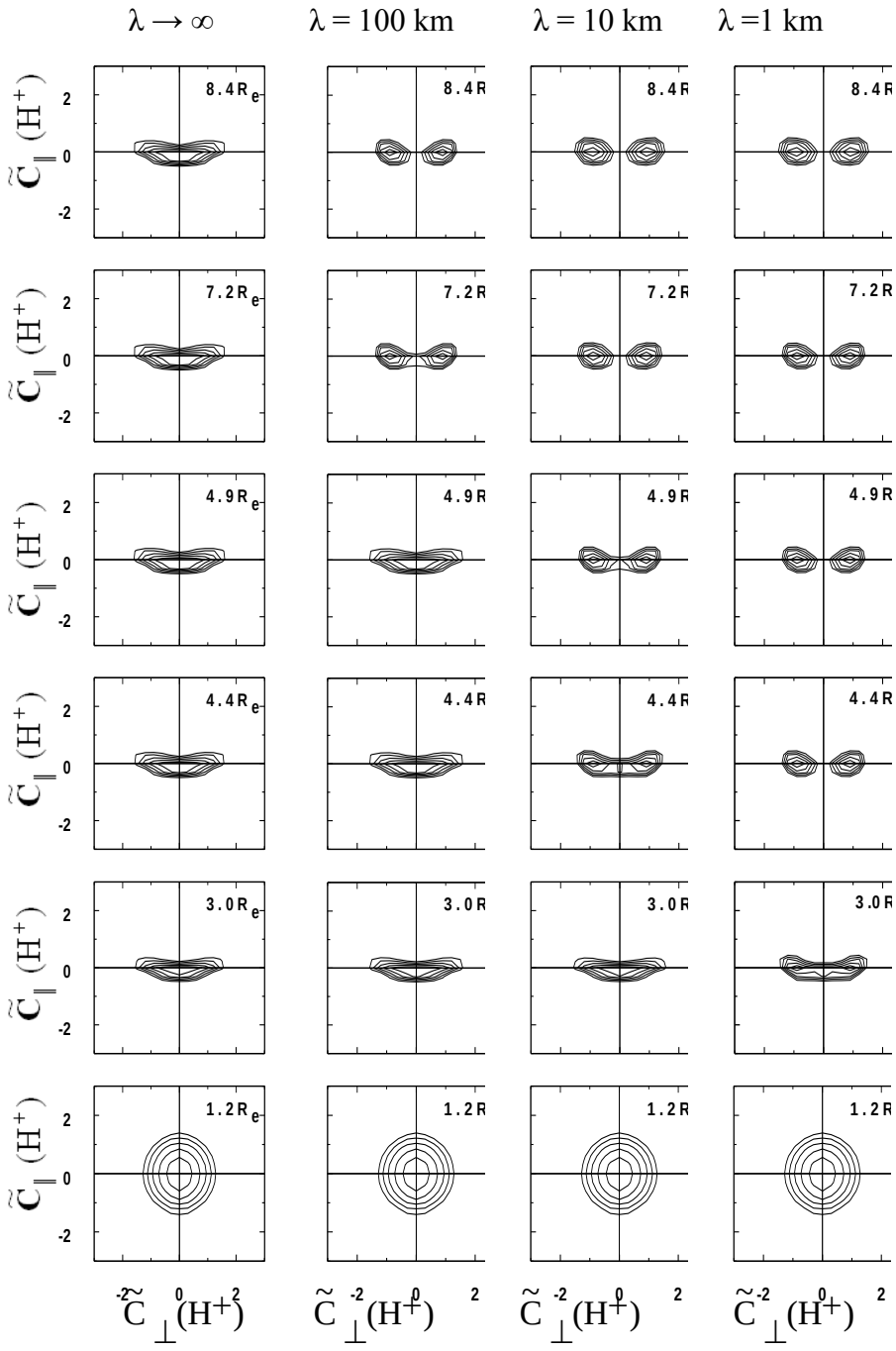


**Figure 4.9:** $H^+$ ions velocity distribution functions at different geocentric altitudes (1.2, 3.0, 4.4, 4.9, 7.2 and 8.4 $R_E$) for different electromagnetic turbulence wavelengths ($\lambda_\perp$), the wavelengths considered here are $\lambda_\perp \to \infty$ (1st panel), $\lambda_\perp = 100\ km$ (2nd panel). $\lambda_\perp = 10\ km$ (3rd panel), and $\lambda_\perp = 1\ km$ (4th panel). $f\left(\mathrm{H}^+\right)$ is represented by equal values contours in the normalized velocity ($\tilde{c}_\parallel, \tilde{c}_\perp$) plane, where $\tilde{\mathbf{c}} = \left[\mathbf{v} - \mathbf{u}(\mathrm{H}^+)\right] / \left[2kT\left(\mathrm{H}^+\right)/m\left(\mathrm{H}^+\right)\right]^{1/2}$. The contour levels decrease successively by a factor $e^{1/2}$ from the maximum.

As ($\lambda_\perp$) decreases, the argument ($\frac{\bar{a}}{\lambda_\perp}$) approaches (one) at low altitudes and consequently, the toroidal distribution appears at lower altitudes, namely for the case ($\lambda_\perp = 10\,Km$) at altitude ($4.9R_E$), the toroidal features become obvious at altitude ($\sim 7.2R_e$) (3rd panel). Moreover, for the case ($\lambda_\perp = 1\,Km$) the toroidal features appear at a lower altitude ($3R_E$) but become obvious at altitude ($4.4R_E$)(4th panel). .For the cases ($\lambda_\perp = 100\ Km$, $\lambda_\perp = 10\ Km$ and $\lambda_\perp = 1\ Km$), the $H^+$ velocity distribution function saturates after forming the toroidal shape, because the perpendicular heating becomes negligible.

We see in the Figure 4.10 the altitude profiles are given for $H^+$ moments ($\lambda_\perp \to \infty$ (solid), $\lambda_\perp = 100\,Km$ (dashed), $\lambda_\perp = 10Km$ (dotted) and $\lambda_\perp = 1\,Km$ (dotted dashed)). The drift velocity (top right) of $H^+$ ions increases with altitude, due to the effect of WPI and heating in the perpendicular direction, which increases the upward mirror force, and so increases the acceleration in the upward direction.

However, we see that the drift velocity at low altitudes are superimposed, because the argument ($\frac{\bar{a}}{\lambda_\perp}$) is less than unity. For the case ($\lambda_\perp = 100\,Km$), the acceleration rate decreases, and so $u(H^+)$ decreases above the saturation point which occurs at altitude ($\sim 7.2\,R_E$) in comparison with the case ($\lambda_\perp \to \infty$), and this is obvious result of the energization's self-limiting nature which occurs when ($\frac{\bar{a}}{\lambda_\perp}$) exceeds unity. For the case ($\lambda_\perp = 10\,Km$), we see that the saturation level appears obvious earlier ($4..4\,R_E$), as $\lambda_\perp$ decreases more and more (i.e. $\lambda_\perp = 1\,Km$), the saturation level appears at lower altitude ($4.4R_E$). These results have a close agreement with the distribution function results displayed in Figure 4.1.

To study the behavior of the $H^+$ density, $n(H^+)$ under the effect of finite $\lambda_\perp$, we first return and set the following argument. For the range of ($\lambda_\perp \geq 1\text{Km}$) considered here, the finite $\lambda_\perp$ effect occurs at relatively high altitude ($\geq 3.0R_E$) where the kinetic energy of the ion becomes more than the energy needed to escape and cross the potential barrier, going to upward direction, therefore, $u(H^+)$ is trans-sonic, and since the $H^+$ ions are in the flux-limiting flow condition, a corresponding decrease in the ions density is expected to compensate for the increase in the ions drift velocity, and hence to keep the net escape flux constant. As $\lambda_\perp$ decreases the increased scale height starts at lower altitudes, which is consistent with $u(H^+)$.

The behavior of $H^+$ ions perpendicular temperature $T_\perp(H^+)$ (left bottom) is a result of balance between WPI heating affecting in the perpendicular direction and perpendicular adiabatic cooling; but $T_\perp(H^+)$ is increasing monotonically with altitude; which means that at high altitudes the effect WPI is greater than that of adiabatic cooling. The profiles of parallel temperature $T_\parallel(H^+)$ (right bottom) is influenced by WPI, where as $H^+$ ions perpendicular heating increases, part of this energy is transferred to the parallel direction, and consequently, the parallel temperature increases. However, as $T_\perp(H^+)$ decreases due to the effect of finite Larmor radius this on the other hand decreases the $H^+$ parallel temperature.

But in general, we see that $T_\perp(H^+)$ and $T_\parallel(H^+)$ display much more changes with $\lambda_\perp$ than $n(H^+)$ and $u(H^+)$.

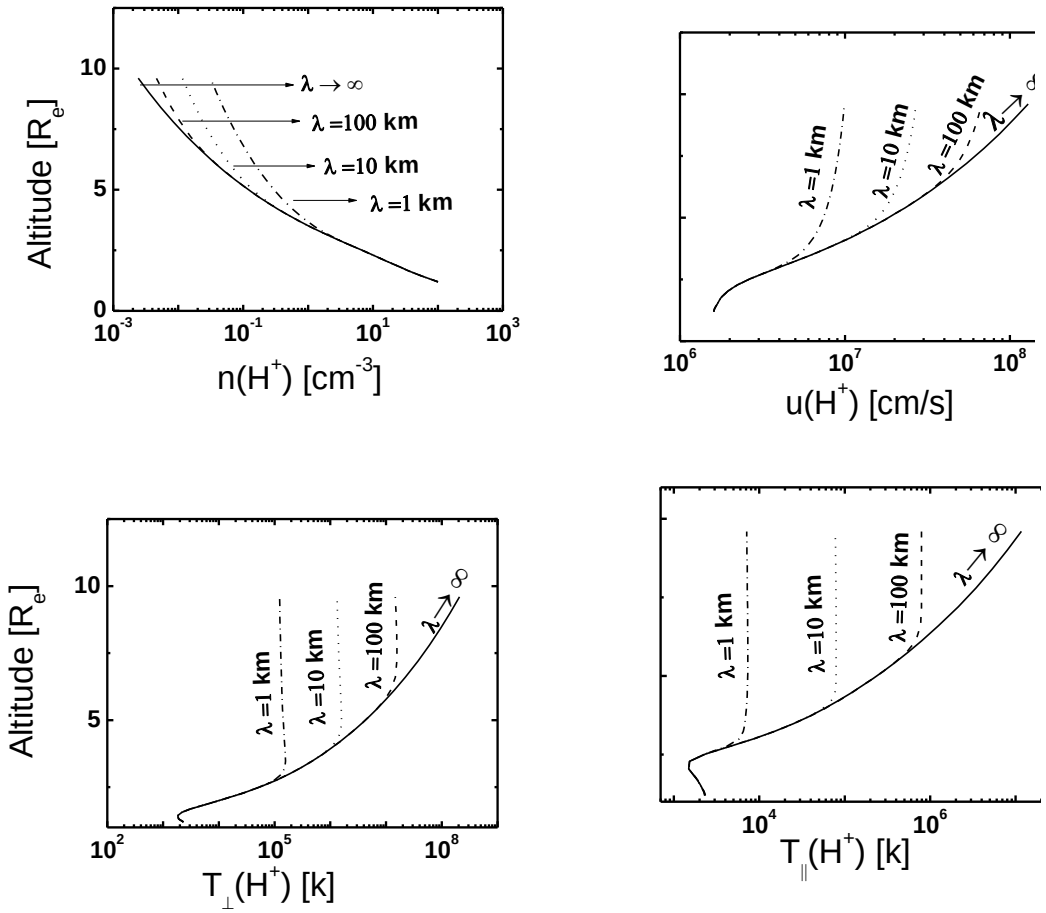


**Figure 4.10:** Altitude profiles of the lower order $H^+$ moment for different electromagnetic turbulence wavelengths ($\lambda_\perp$). The wavelengths considered here are $\lambda_\perp \to \infty$ (solid), $\lambda_\perp = 100\ Km$ (dashed). $\lambda_\perp = 10\ Km$ (dotted) $\lambda_\perp = 1 Km$ (dashed dotted). The $H^+$ moments considered here are: density $n(H^+)$ (top left), drift velocity $u(H^+)$ (top right), perpendicular temperature $T_\perp(H^+)$ (bottom left), and parallel temperature $T_\parallel(H^+)$ (bottom right).

### 4.3.2 $O^+$ ions

To study the effect of finite Larmor radius on the $O^+$ ions, they computed the distribution function $f(O^+)$ at different altitudes extended from ($1.2\,R_E$ to $9.6\,R_E$) for

different values of $\lambda_\perp$, they assumed a wide range of $\lambda_\perp$ which are the same in the $H^+$ ions case ($\lambda \to \infty$ case ($1^{st}$ panel), $\lambda_\perp = 100\,Km$ ($2^{nd}$ panel), $\lambda_\perp = 10\,Km$ ($3^{rd}$ panel), and $\lambda_\perp = 1\,Km$ ($4^{th}$ panel)) but in addition to the assumption $\lambda \to \infty$ case ($1^{st}$ panel),as mentioned in [Barghouthi 1997], the Figure 4.11 shows the shapes of the distribution function.

For the case $\lambda_\perp = 100\,Km$, the behavior of ions remains the same as the case of $\lambda \to \infty$ up to altitude $3.0R_E$, where as the toroidal features appear at altitude ($\sim 4.0R_E$), and saturated above that level ($1^{st}$ and $2^{nd}$ panels). For the case $\lambda_\perp = 10\,Km$ the distribution functions behaves as in the case of $\lambda_\perp = 100\,Km$, only toroidal distribution function appears at lower altitude (i.e. $3.0R_E$). However, for $\lambda_\perp = 1Km$, the toroidal feature appears at lower altitudes, it starts to appear at altitude ($2.0R_E$) and becomes well established at altitude $2.3R_E$ ($4^{th}$ panel). As mentioned before, the toroidal distribution feature can be explained since ($D_\perp$) peaks near ($v_\perp = 0$), and decreases rapidly for large values of ($v_\perp$); therefore, the ions tend to move out of the region of large diffusion ($v_\perp \cong 0$) and accumulate in the region of relatively low ($D_\perp$) forming the aforementioned toroidal distribution function.

The differences between the behavior of $H^+$ and $O^+$ under the effect of finite Larmor radius comes from two factors. Firstly, the mass of $H^+$ ion is much small comparable to that of $O^+$ ion ($m(H^+) = \frac{1}{16} m(O^+)$), and secondly, the preferential heating of $O^+$ ion seemed at lower altitudes, and so the saturation levels occur earlier because of the self-limiting heating.

Figure 4.12 shows the profiles of moments of $O^+$ ions, we see that the behavior of $O^+$ ions for each profile at low altitudes (i.e. $2.0R_E$) coincide for all the values of

$\lambda_\perp$ which are ($\lambda \to \infty, 100\,Km, 10\,Km$, and $1\,Km$), that is due to the argument ($\frac{\bar{a}}{\lambda_\perp}$) is less than unity. For example, the drift velocity $u(O^+)$ (top right) decreases due to the reduction of the heating rate, and the density $n(O^+)$ (top left) increases to keep the escape flux constant. And also as $\lambda_\perp$ decreases, the growth rate of $T_\perp(O^+)$ (bottom left) and so $T_\parallel(O^+)$ (bottom right) is reduced because of the significant reduction in the heating rate above the saturation levels. In generally, the saturation level appears at low altitudes for small values of $\lambda_\perp$ , namely, at about $2.3R_E$ for $\lambda_\perp = 1\,Km$, $3.0R_E$ for $\lambda_\perp = 10\,Km$, $4.0R_E$ for $\lambda_\perp = 100\,Km$, and $> 10R_E$ for $\lambda \to \infty$, and this is also in agreement with the distribution functions in the Figure 4.5.

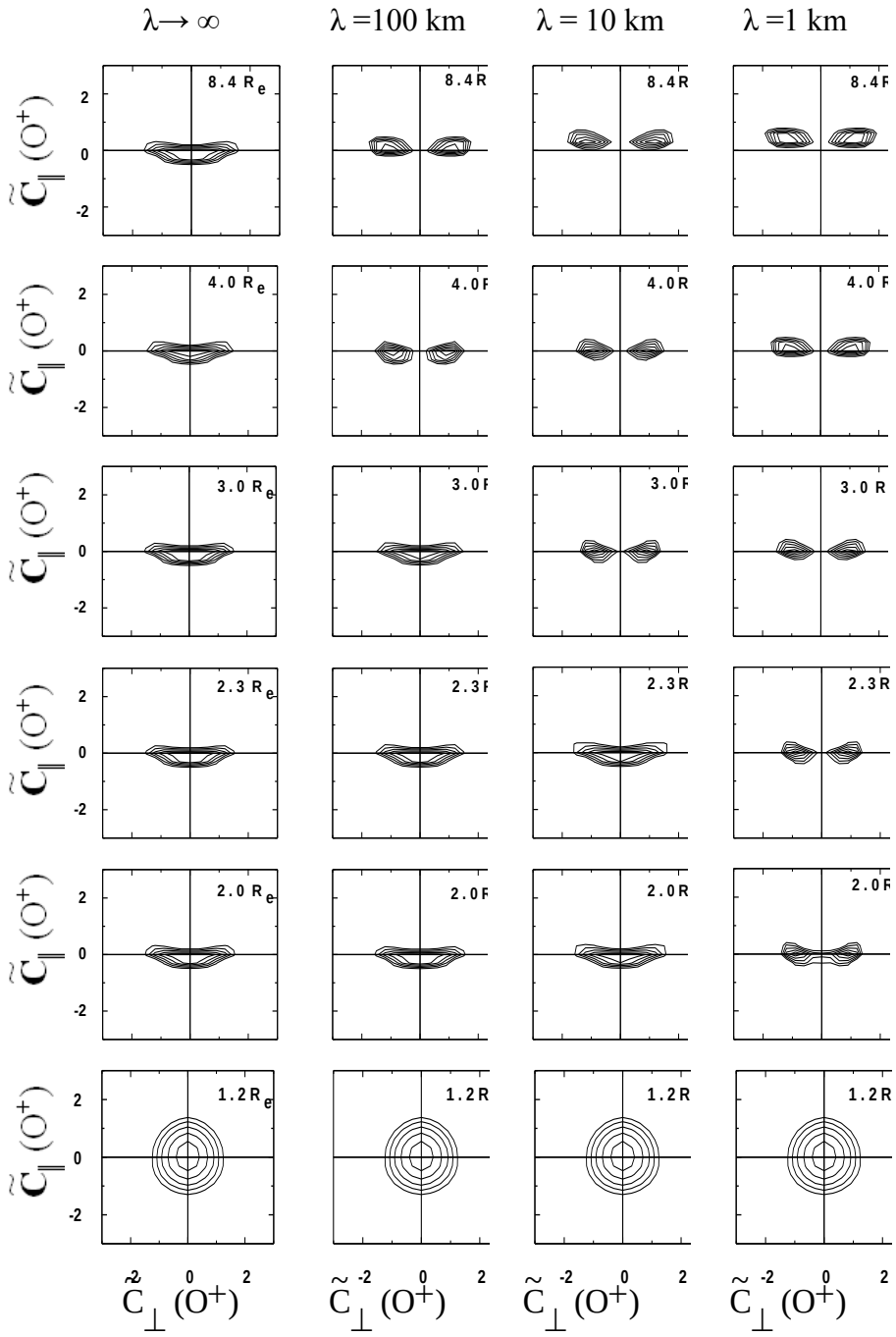


**Figure 4.11:** $O^+$ ions velocity distribution functions at different geocentric distances (1.2, 2.0, 2.3, 3.0, 4.0, and 8.4 $R_E$) for different electromagnetic turbulence wavelengths ( $\lambda_\perp$ ), the wavelengths considered here are $\lambda_\perp \to \infty$ (1st panel). $\lambda_\perp = 100\ Km$ (2nd panel). $\lambda_\perp = 10\ Km$ (3rd panel) $\lambda_\perp = 1 Km$ (4th panel). $f\left(\mathrm{O}^+\right)$ is represented by equal values contours in the normalized velocity ( $\tilde{c}_\parallel$ , $\tilde{c}_\perp$ ) plane, where $\tilde{\mathbf{c}} = \left[\mathbf{v} - \mathbf{u}(\mathrm{O}^+)\right] / \left[2kT\left(\mathrm{O}^+\right)/m\left(\mathrm{O}^+\right)\right]^{1/2}$. The contour levels decrease successively by a factor $e^{1/2}$ from the maximum.

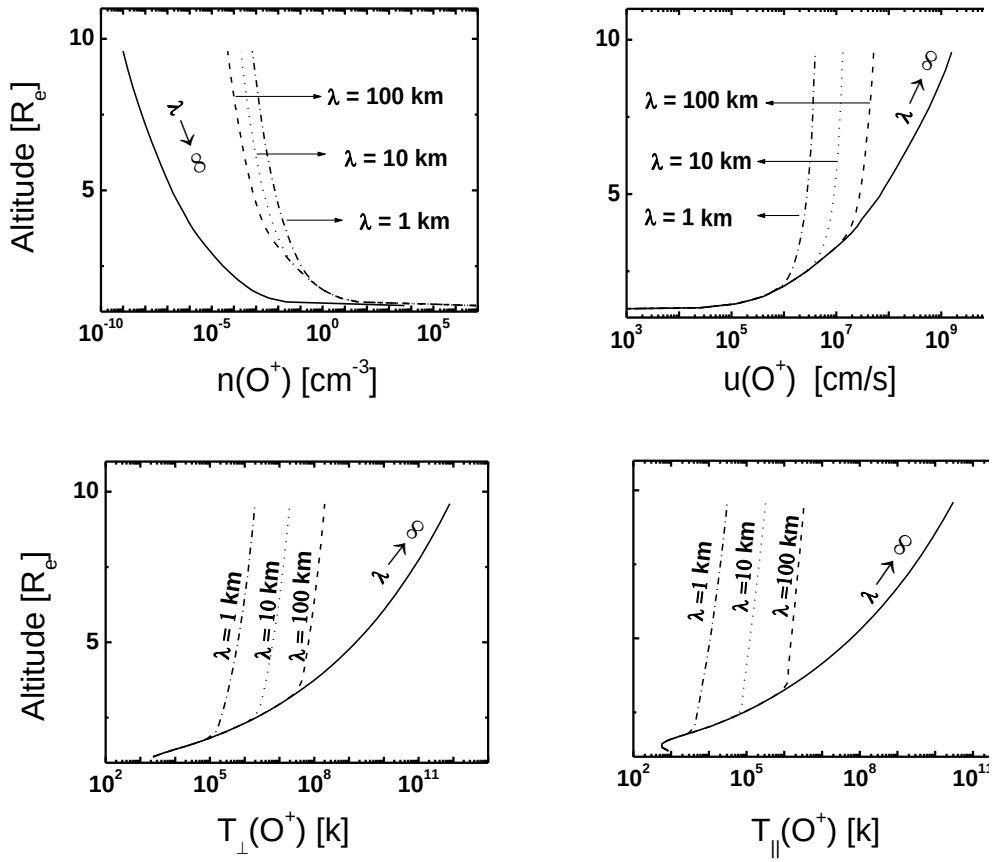


**Figure 4.12:** Altitude profiles of the lower order $O^+$ moment for different electromagnetic turbulence wavelengths ($\lambda_\perp$). The wavelengths considered here are $\lambda_\perp \to \infty$ (solid), $\lambda_\perp = 100\ Km$ (dashed), $\lambda_\perp = 10\,Km$ (dotted), $\lambda_\perp = 1\ Km$ (dashed dotted). The $O^+$ moments considered here are: density $n(O^+)$ (top left), drift velocity $u(O^+)$ (top right), perpendicular temperature $T_\perp(O^+)$ (bottom left), and parallel temperature $T_\parallel(O^+)$ (bottom right).

# Chapter Five

# Comparisons and Conclusions

# Chapter Five

# Comparisons and Conclusions

## 5.1. Comparison between the Simulation Results and Observations

The MC simulation was run for the three models with different forms of $D_{\perp}(r, v_{\perp})$, i.e. equations (2.25 and 2.26) for RCC model, equation (2.28) for Bouhram model, and equation (2.30) for Barghouthi model. For the sake of comparison we chose to present part of the previous models results for $\lambda_{\perp}$=10 km, because these results represent the closest results to the observations. Figures 5.1 and 5.2 present the $H^+$ and $O^+$ ion velocity distributions at 4.8 $R_E$, respectively. The form of the ion velocity distribution is determined by the competition of the transverse ion acceleration and magnetic mirroring processes. Wave-particle interactions of the ambient ion population with the electromagnetic turbulence near $\Omega$ leads to ion acceleration in the perpendicular direction, which is followed by adiabatic cooling (folding) of velocities as the ions mirror and travel up the geomagnetic field lines to create ion conic at low altitude ( ~ 2 $R_E$ ) as shown by [Barghouthi and Atout, (2006)]. However, $H^+$ and $O^+$ ions tend to move out of the region of large $D_{\perp}(r, v_{\perp})$ and accumulate in the region of relatively low $D_{\perp}(r, v_{\perp})$ to form toroids at high altitudes [Barghouthi and Atout, 2006]. At 4.8 $R_E$, the above tested models produced the toroids; however the simulation results of Barghouthi model are closer to the observed toroids for both $H^+$ and $O^+$ ions as shown in Figures 5.1 and 5.2 respectively.

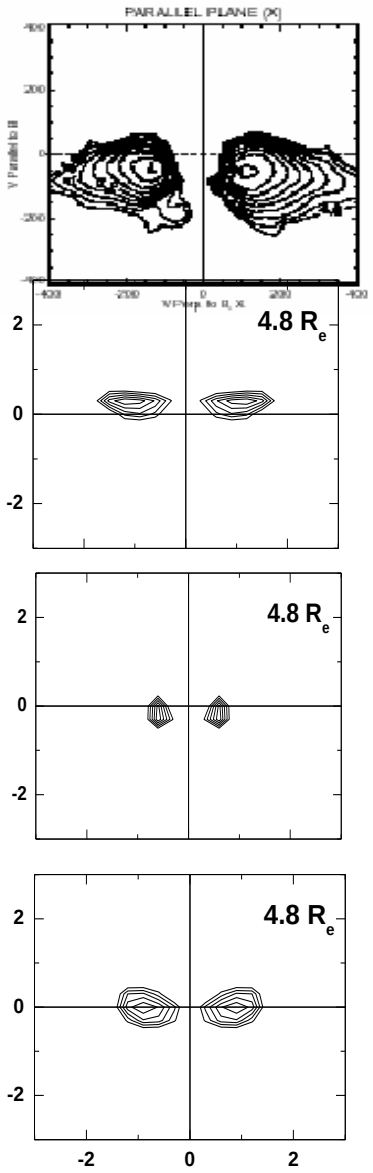


**Figure 5.1:** The top panel presents the observed $H^+$ ions velocity distribution [Huddleston et al. 2000], while the other ion velocity distributions represent the theoretical $H^+$ ion velocity distributions for different wave-particle interactions models, RCC model, Bouhram model ( $\lambda_\perp = 10Km$), and Barghouthi model ( $\lambda_\perp = 10Km$) at 4.8 $R_E$. Where $\tilde{\mathbf{c}} = \left[\mathbf{v} - \mathbf{u}(\mathrm{H}^+)\right] / \left[2kT\left(\mathrm{H}^+\right) / m\left(\mathrm{H}^+\right)\right]^{1/2}$.

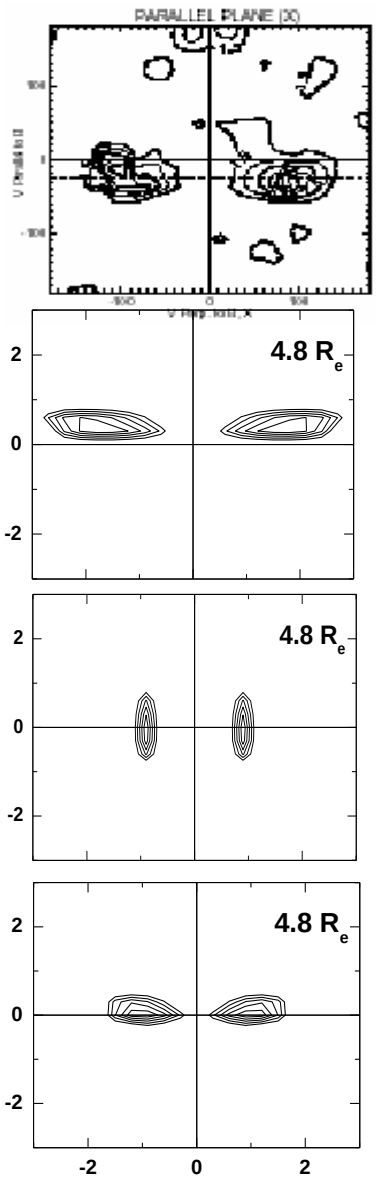


**Figure 5.2:** The top panel presents the observed $O^+$ ions velocity distribution [Huddleston et al., 2000], while the other ion velocity distributions represent the theoretical $O^+$ ion velocity distributions for different wave-particle interactions models, RCC model, Bouhram model ( $\lambda_\perp = 10Km$), and Barghouthi model ( $\lambda_\perp = 10Km$) at 4.8 $R_E$. Where $\tilde{\mathbf{c}} = \left[\mathbf{v} - \mathbf{u}(\mathrm{O}^+)\right] / \left[2kT(\mathrm{O}^+)/m(\mathrm{O}^+)\right]^{1/2}$.

According to RCC model, the peaked nature of the diffusion coefficient $D_\perp$ (equations (2.25 and 2.26)) reflects the way in which wave-particle interactions lead

to the formation of ion toroids. Because $D_\perp$ falls to zero at small perpendicular velocities ($i.e\, v_\perp << v_\circ$), the bulk of the ion velocity distribution is unaffected by interaction with the waves (electromagnetic turbulence).

As $v_\perp$ increases and becomes near $v_\circ$, $D_\perp$ begins to become appreciable and very significant, respectively, and the diffusion process begins to affect the $H^+$ ions in the distribution by heating them in the perpendicular direction. Above the peak, when $v_\perp >> v_\circ$, the diffusion coefficient $D_\perp$ decreases very rapidly as $(v_\perp / v_\circ)^{-3}$ and consequently, the effect of wave–particle interactions becomes negligible. Because there are initially more ions at lower velocities than at higher velocities, the net escape flux in velocity space is toward higher velocities, leading to the formation of toroids. In other words, the ions tend to move out of the region of large diffusion ( $v_\perp \approx v_\circ$) and accumulate in the region of relatively low $D_\perp$ ( $v_\perp >> v_\circ$) forming the aforementioned toroidal ion velocity distributions "Donuts".

According to Bouhram model, the toroidal shape can be explained if we remember that $D_\perp$ (equation (2.28)) peaks near $v_\perp \cong 0$, and decreases very rapidly as $J_0^2\left(\frac{k_\perp v_\perp}{\Omega_i}\right)$ for large values of $v_\perp$; therefore, the ions tend to move out of the region of large diffusion coefficient and accumulate in the region of relatively low $D_\perp$, forming the aforementioned toroidal distributions.

According to Barghouthi model, the formation of ion toroids can be explained if we remember that $D_\perp$ (equation (2.30)) peaks near $k_\perp v_\perp / \Omega = 1$ and decreases rapidly for large values of $k_\perp v_\perp / \Omega$. Therefore the ions ($H^+$ or $O^+$) tend to move out of the region of large diffusion $(k_\perp v_\perp / \Omega < 1)$ and accumulate in the region of relatively low $D_\perp$ $(k_\perp v_\perp / \Omega > 1)$ forming the aforementioned toroidal distributions.

## 5.2. Conclusions

A Monte Carlo simulation was used to study the effects of altitude and velocity dependent wave-particle interactions on $O^+$ and $H^+$ ions outflows in the Auroral region. The model also included the effects of gravity, polarization electrostatic field, and diverging geomagnetic field. The ion's perpendicular heating was modeled by developing a form for the diffusion coefficient $D_\perp$ as a function of perpendicular velocity $v_\perp$ and position ($r/R_E$) along the Auroral geomagnetic field line.

According to RCC model and for the velocity dependence of $D_\perp$ , we chose the form obtained by [Crew and Chang, 1985], while for spatial variation we chose the form calculated by [Barghouthi, 1997]. We found that, as a result of including the velocity dependence wave-particle interactions, in addition to the altitude dependent WPI, the $O^+$ and $H^+$ ions velocity distributions displayed toroidal features at altitudes greater than ~ 3 $R_E$, because ions tend to move out of the heating zone into a region of negligible WPI, and we explained this in terms of the peaked nature of the diffusion coefficient. Also, including the effect of velocity dependent WPI produced realistic ion temperatures that are comparable to observations. Also, for the case of altitude dependent and velocity independent WPI, the diffusion coefficient $D_\perp$ increases, monotonically, with altitude and consequently, the strength of WPI increases with altitude, however, for the case of altitude and velocity dependent WPI, the variation of $D_\perp$ is very important and crucial. As $v_\perp$ goes to zero, $D_\perp$ goes to zero as $(v_\perp / v_\circ)^{-1}$; and at velocities much larger than $v_\circ$, $D_\perp$ falls as $(v_\perp / v_\circ)^{-3}$, this peaked nature of $D_\perp$ reflects the way in which altitude and velocity dependent wave-particle interactions lead to the formation of $O^+$ and $H^+$ toroids. Because $D_\perp$ falls to zero at small velocities, the bulk of the ion velocity

distribution is unaffected by the interaction with the waves. Near velocity $v_\circ$, $D_\perp$ begins to become appreciable, and the diffusion process begins to affect ions in the distributions. Because there are more ions at lower velocity than at higher velocity, the net escape flux in velocity space is toward higher velocities, leading to the formation of toroids. For $v_\perp >> v_\circ$, $D_\perp$ falls to zero, and this turns the role of WPI to be negligible and consequently, the ions in the "Donuts" are unaffected by WPI, i.e., the ion heating process turned to be self-limiting.

According to Bouhram model, the effect of altitude and velocity dependent wave-particle interactions on $O^+$ and $H^+$ ions outflows was studied for conditions representative of the Auroral region using a MC simulation. In addition to the altitude and velocity dependent wave-particle interaction, we considered the body force (gravitational and polarization electrostatic) and the divergence of geomagnetic field lines. The following conclusion are drawn:

(1) At low altitudes, the argument $(\frac{k_{\perp\circ} v_\perp}{\Omega_i})$ was much less than unity and, consequently the results were independent of $\lambda_\perp$. Above a certain point called saturation point, the argument $(\frac{k_{\perp\circ} v_\perp}{\Omega_i})$ became larger than unity and the heating rate turned to be very negligible.

(2) Below the saturation point, the $O^+$ and $H^+$ ions velocity distributions displayed a conic features due to the effects of perpendicular heating and mirror force.

(3) Above the saturation points, $O^+$ and $H^+$ velocity distribution displayed toroidal features, because the ions tend to diffuse out of the heating region in the velocity space.

(4) The ion heating rate is dramatically decreased above the saturation point, because of the velocity dependence of $D_{\perp}$ on $J_{\circ}^{2}(\frac{k_{\perp\circ}v_{\perp}}{\Omega_i})$.

(5) As the electromagnetic turbulence wavelength $\lambda_{\perp}$ decreases, the ion heating rate decreased and the saturation point occurred at lower altitudes.

(6) The saturation points of $O^+$ ions occurred at lower altitudes than those of $H^+$ ions.

The main effect of finite electromagnetic turbulence wavelength $\lambda_{\perp}$ on $O^+$ and $H^+$ outflows at high-altitude and high-latitude is to produce $O^+$ and $H^+$ toroids at the saturation point and to decrease the heating rate above the saturation point consequently, for large values of $\lambda_{\perp}$ the effect of wave-particle interactions turned to be not important, and then the ion outflow can be described by Liouville theorem.

Finally, the different forms of velocity diffusion coefficient, $D_{\perp}(r, v_{\perp})$ (RCC model, Bouhram model, and Barghouthi model), have been used in the MC simulation to obtain $O^+$ and $H^+$ ions velocity distributions at high altitudes in the equatorward region of the cusp. The results of these models have been compared with the corresponding observations of [Huddleston *et al.,* (2000)]. As a result of comparison, we have found an excellent agreement between the observations and the MC calculations obtained by Barghouthi model.

# References


Arvelius, S.,Yamauchi, M., Nilsson, H., Lundin, R., Hobara, Y., Reme, H., Bavassano-Cattaneo, M. B., Paschmann, G., Korth, A., Kistler, L. M., and Parks, G. K.: Statistics of high-altitude and high-Latitude $O^+$ ion outflows observed by Cluster/CIS, Ann. Geophys, 23, 1909 -1916, 2005.

Arnoldy, R. L., Lynch, K. A., Kintner, P. M., Vago, J. L., S. W. Chesney, S. W., Moore, T., and Pollock, C.: Burst of transverse ion acceleration at rocket altitudes, Geophys. Res. Lett., 19, 413-416, 1992.

Axford, W. I., The polar wind and the terrestial helium budget, J. geophys. Res., 73,6855,1968.

Barakat, A. R. and I. A. Barghouthi, The effects of wave-particle interactions on the polar wind $O^+$, Geophys. Res. Lett., 21 2279-2282. 1994a.

Barakat, A. R. and I. A. Barghouthi, The effects of wave-particle interactions on the polar wind: Preliminary results, Planet. Space Sci., 42, 987-992, 1994b.

Barakat, A. R., and R. W. Schunk, Comparison of Maxellian and bi-Maxwellian expansions with MC simulations for anisotropic Plasmas, J. phys. D., 15, 2189,1982c.

Barakat, A. R., and R. W. Schunk, $O^+$ ions in the polar wind, J. Geophys. Res., 88, 7887-7894,1983.

Barakat, A. R., and R. W. Schunk, Stability of $H^+$ beams in the polar wind, J. Geophys. Res., 94,1487-1494,1989.

Barghouthi I. A., Effects of wave particle interactions on $H^+$ and $O^+$ outflow at high latitude; A comparative study, J. Geophys. Res., 102, 22. 062-22.075, 1997.

Barghouthi, I. A., and Atout, M. A.: MC modeling of toroidal ion distributions and ion temperatures at high altitudes equatorward of the cusp: Effect of finite gyroradius, J. Geophys. Res., 111, A03202, 2006.

Barghouthi, I. A., and Barakat A. R.: Comparison between the wave- particle interaction in the polar wind and in the Auroral region, Physics of Space Plasmas, 13, 445-450, 1995.

Barghouthi I. A., A. R. Barakat, A. M. Persoon, The effects of altitude –dependent wave particle interactions on the polar wind plasma, Astrophysics and space sciences, 259, 117, 1998.

Barghouthi I. A., N. A. Qatanani, M.S. Abu Issa, Toroidal distributions in the polar wind plasma; Indian j.phys. 77B (6), 621-625, 2003a.

Barghouthi I.A., N.A. Qatanani, F. M. Allan, MC simulation of Boltzmann equation in space plasma at high latitude latitudes, MC Methods and Appl., 9, 3, 201-216, 2003b.

Bauer, S. J., The structure of the topside ionosphere, Electron Density profiles in Ionosphere and Exosphere, edited by J. Frihagen, North-Holland, New York, p. 387, 1966.

Biddle, A.P., T.E. Moore, C.R. Chappell. Evidence for ion heat flux in the light ion polar wind. Journal of Geophysical Research 90, 8552-8558, 1985.

Bouhram, M., Dubouloz, N., Malingre, M., Jasperse, J. R., Pottelette, R., Senior, C., Delcourt, D., Carlson, C.W., Roth, I., Berthomier, M., and Sauvaud, J. A-.: Ion outflow and associated perpendicular heating in the cusp observed by Interball Auroral Probe and Fast Auroral Snapshot, J. Geophys. Res., 107, 10.1029/ 2001 JA 000091., 2002.

Bouhram, M., Klecker, B., Miyake, W., Reme, H., Sauvaud, J. –A., Malingre, M., Kistler, L., and Blagau, A.: On the altitude dependence of transversely heated $O^+$ distributions in the cusp/cleft, Annales Geophys., 22, 1-12, 2004.

Bouhram, M., Malingre, M., Jasperse, J. R, and Dubouloz, N.: Modeling transverse heating and outflow of ionospheric ions from the dayside cusp/clef: 1 A parametric study, Ann. Geophys. 21, 1753-1771, 2003a.

Bouhram, M., Malingre, M., Jasperse, J. R, and Dubouloz, N., and Sauvaud, J. –A.: Modeling transverse heating and outflow of ionospheric ions from the dayside cusp/clef: 2 Applications, Ann. Geophys. 21, 1773-1791, 2003b.

Chang, T.. Lower-hybrid collapse, Caviton turbulence, and charged particle energization in the topside Auroral ionosphere and magnetosphere. Physics of Fluids B 5(7), 2646-2656, 1993.

Chang, T., Coppi, B.: Lower hybrid acceleration and ion evolution in the suprAuroral region, Geophys. Res. Lett., 8, 1253 – 1256, 1981.

Chang, T., G. B. Crew, N. Hershkowitz, J. R. Jasperse, J. M. Retterer, J. D. Winningham. Transverse acceleration of oxygen ions by electromagnetic ion cyclotron resonance with broadband left-hand polarized waves. Geophysical Research Letters 13, 636 – 639, 1986.

Crew, G. B., T. Chang. Asymptotic theory of ion conic distributions. Physics of Fluids 28(8), 2382-2394, 1985.

Crew, G. B., Chang, T., Retterer, J. M., Peterson, W. K., Gurnett, D. A., Huff, R. L.: Ion cyclotron resonance heated conics: Theory and observations. Journal of Geophysical Research 95, 3959 – 3985, 1990.

Davies, Kenneth, Ionospheric Radio, Peter Peregrinus Ltd .London , 1990.

Desseler, A. J., and F. C. Michel, Plasma in the geomagnetic tail, J. Geophys. Res., 71, 1421, 1966.

Eklund, U., Lundin, R., and Sandahl, I.: Measurements of $O^+$ in the high latitude magnetosheath, Phys. Chem. Earth., 22, 639 – 644, 1997.

Gurnett, D. A., and U. S. Inan, Plasma wave observations with the Dynamic explorer 1 spacecraft, Rev. Geophys., 26, 285-316, 1988.

Ho, C .W., J. L . Horwitz and T. E. Moore 1994, DE1 observation of polar $O^+$ stream bulk parameters and comparison with a model of the centrifugal-accelerated polar wind, *Geophys. Res. Lett., 21* , 2459 – 2462, 1994.

Horita, R.E., A. W. Yau, B. A. Whalen, T. Abe, S. Watanabe. Ion depletion zones in the polar wind – EXOS D suprathermal ion mass spectrometer observations in the polar cap. Journal of Geophysical Research 98, 11,439 – 11,448, 1993.

Huddleston, M. M., C. J. Pollock, M.P.Wuest, J. S. Pichett, T. E. Moore, and W. K. Peterson, Toroidal ion distributions observed at high altitudes equatorwardof the cusp, Geophysical, Research Letters, 27, 4, 469-472, 2000.

Klumpar, D. M., Peterson, W. K., and Shelley, E. G.: Direct evidence for two- stage (bimodal) acceleration ionospheric ions, J. Geophys. Res. 89, 10779-10787, 1984.

Lemaire, J. F., W. K. Peterson, T. Chang, R. W. Schunk, A. R. Barakat, H. G. Demars, G. V. Khazanov. History of kinetic polar wind models and early observations. Journal of Atmospheric Solar – Terrestrial Physics, 121, 427-489, 2007.

Lundin, R., Woch, J., Yamauchi, M., and Marklund, G.: Boundary Layer polarization and voltage in the 14 MLT regions, J. Geophys. Res., 100, 7587-7597, 1995.

Moore, T. E., C. R. Cahppell, M. Lockwood, and J. H. Waite Jr., Super thermal ion signature of Auroral acceleration processes, J.Geophes. Res., 90. 1611-1618, 1985.

William J., Kaufmann III, F. Neil, Discovering the Universe, Fourth edition, New York, 1987.

Moore, T. E., Lundin, R., Alcayde, D., Andre', M., Ganguli, S. B., Temerin, M., and Yau, A.: Source processes in the High-Latitude ionosphere, Space Sci. Rev, 88, 7, 1999.

Nagai, T., J.H. Waite, J. L. Green, C. R. Chappell. First measurements of supersonic polar wind in the polar magnetosphere. Geophysical Research Letters 11, 669 -672, 1984.

Persoon, A. M., D. A. Gurnett, S. D. Shawhan. Polar cap electron densities from DE-1 plasma wave observations. Journal of Geophysical Research 88, 10,123-10, 136, 1983.

Peterson, W.K.. On the energy sources responsible for the escape of heavy ions from the ionosphere. Physics of Space Plasmas, SPI Conf. Proc. And Reprint Ser., Vol 14, edited by T. Chang and J. R. Jasperse, Scientific, Cambridge Mass, 1995.

Retterer, J. M., Chang, T., Jasperse, J. R.: Transversely accelerated ions in the topside ionosphere. J. Geophys. Res., 99, 13,189 – 13,201, 1994.

Retterer, J. M., T. Chang, G. B., Crew, J. R. Jasperse, and J. D. Winningham, MC modeling of oxygen ion conic acceleration by cyclotron resonance, phys. Rev. Lett., 59, 148-151, 1987a.

Retterer, J. M., T. Chang, G. B., Crew, J. R. Jasperse, and J. D. Winningham, MC modeling of oxygen ion conic acceleration by cyclotron resonance with broadband electromagmetic turbulence, in physics of space plasma, SPI Conf. Proc. andReprint Ser.,No. 6,edited by T. Chang , J. Belcher, J. R. Jasperse, and G. Crew, Scientific, Cambridge, Mass., pp.97-111, 1987b.

Retterer, J. M., Chang, T., and Jasperse, J. R.: Ion acceleration by lower hybrid waves in the suprAuroral region, J. Geophys. Res., 91, 1609-1618, 1986.

Robert, H. Eather, Majestic Lights, American Geophysical Union, Washington D.C., 1980.

Schunk, R. W., Mathematical structure of transport equations for multispecies flows, Rev. Geophys., 15, 429, 1977.

Schunk, R. W. and A. F. Nagy, Ionospheres: physics plasma physics, and chemistry, First published, Cambridge University Press, Cambridge, 2000.

Theodore P. Snow, The Dynamic Universe, Fourth Edition, West Publishing Company, New York. 1993.

Tsurutani, B. T. and G. S. Lakhina, Some concepts of wave- particle interactions in the collisionless plasmas, Reviews of Geophysics, 35, 4, 491-502, 1997.

Winningham, J. D., and Burch, J.: Observations of large-scale ion conic generation with DE-1, Physics of Space Plasmas, *5*, 137-158, 1984.

Yau, A. W., B. A. Whalen, T. Abe, T. Mukai, K. I. Oyama, T. Chang. Akebono observations of electron temperature anisotropy in the polar wind. Journal of Geophysical Research, 100, 17,451, 1995.

http://www.phy6.org/Education/wstern.html (23/3/2006)

http://www.albany.edu/faculty/rgk/atm101/Aurora.htm (19/3/2006)

http://ssdoo.gsfc.nasa.gov/education/lectures/fig05.gif (10/3/2006)

http://en.wikipedia.org/wiki/Image:Magnetosphere_schematic.jpg (11/3/2006)